Monthly Notices
of the
ROYAL ASTRONOMICAL SOCIETY

MNRAS **475,** 2097–2121 (2018)
Advance Access publication 2017 December 14

doi:10.1093/mnras/stx3227

HERUS: the far-IR/submm spectral energy distributions of local ULIRGs and photometric atlas

D. L. Clements,[1]★ C. Pearson,[2,3,4] D. Farrah,[5] J. Greenslade,[1]
Jeronimo Bernard-Salas,[3] E. González-Alfonso,[6] J. Afonso,[7,8] A. Efstathiou,[9]
D. Rigopoulou,[2,4] V. Lebouteiller,[10,11] P. D. Hurley[12] and H. Spoon[13]

[1]*Astrophysics Group, Imperial College London, Blackett Laboratory, Prince Consort Road, London SW7 2AZ, UK*
[2]*RAL Space, CCLRC, Rutherford Appleton Laboratory, Chilton, Didcot, Oxfordshire OX11 0QX, UK*
[3]*School of Physical Sciences, The Open University, Milton Keynes MK7 6AA, UK*
[4]*Oxford Astrophysics, Denys Wilkinson Building, University of Oxford, Keble Road, Oxford OX1 3RH, UK*
[5]*Department of Physics, Virginia Tech, Blacksburg, VA 24061, USA*
[6]*Universidad de Alcalá, Departamento de Física y Matemáticas, Campus Universitario, E-28871 Alcalá de Henares, Madrid, Spain*
[7]*Instituto de Astrofísica e Ciências do Espaço, Universidade de Lisboa, OAL, Tapada da Ajuda, P-1349-018 Lisboa, Portugal*
[8]*Departamento de Física, Faculdade de Ciências, Universidade de Lisboa, Edifício C8, Campo Grande, P-1749-016 Lisbon, Portugal*
[9]*School of Sciences, European University Cyprus, Diogenes Street, Engomi, 1516 Nicosia, Cyprus*
[10]*Université Paris Diderot, AIM, Sorbonne Paris Cité, CEA, CNRS, F-91191 Gif-sur-Yvette, France*
[11]*IRFU, CEA, Université Paris-Saclay, F-91191 Gif-sur-Yvette, France*
[12]*Astronomy Centre, Department of Physics and Astronomy, University of Sussex, Falmer, Brighton BN1 9QH, UK*
[13]*Space Sciences Building, Cornell University, Ithaca, NY 14853, USA*

Accepted 2017 December 11. Received 2017 December 11; in original form 2017 September 15

ABSTRACT

We present the *Herschel*-SPIRE photometric atlas for a complete flux limited sample of 43 local ultraluminous infrared galaxies (ULIRGs), selected at 60 μm by *IRAS*, as part of the HERschel ULIRG Survey (HERUS). Photometry observations were obtained using the SPIRE instrument at 250, 350, and 500 μm. We describe these observations, present the results, and combine the new observations with data from *IRAS* to examine the far-infrared spectral energy distributions (SEDs) of these sources. We fit the observed SEDs of HERUS objects with a simple parametrized modified blackbody model, where temperature and emissivity β are free parameters. We compare the fitted values to those of non-ULIRG local galaxies, and find, in agreement with earlier results, that HERUS ULIRGs have warmer dust (median temperature $T = 37.9 \pm 4.7$ K compared to 21.3 ± 3.4 K) but a similar β distribution (median $\beta = 1.7$ compared to 1.8) to the *Herschel* reference sample (HRS, Cortese et al. 2014) galaxies. Dust masses are found to be in the range of $10^{7.5}$–10^9 M$_\odot$, significantly higher than that of HRS sources. We compare our results for local ULIRGs with higher redshift samples selected at 250 and 850 μm. These latter sources generally have cooler dust and/or redder 100-to-250 μm colours than our 60 μm-selected ULIRGs. We show that this difference may in part be the result of the sources being selected at different wavelengths rather than being a simple indication of rapid evolution in the properties of the population.

Key words: galaxies: interactions – galaxies: starburst – infrared: galaxies – submillimetre: galaxies.

1 INTRODUCTION

Ultraluminous infrared galaxies(ULIRGs) are a rare class of objects in the local Universe, which have a far-infrared (far-IR) luminosity (8 to 1000 μm) $> 10^{12}$ L$_\odot$. They were initially discovered by the *IRAS* satellite (Soifer et al. 1984; Wright, Joseph & Meikle 1984) and were then extensively studied through ground-based followup (e.g. Sanders et al. 1988a) and by subsequent space missions (see Sanders & Mirabel 1996, and references therein). Almost all local ULIRGs turn out to be the result of a merger between two gas rich galaxies (e.g. Clements et al. 1996; Rigopoulou et al. 1999; Farrah et al. 2001) and are powered by a major starburst or active galactic nucleus (AGN) activity triggered by this interaction. They

---

★ E-mail: d.clements@imperial.ac.uk

Published by Oxford University Press on behalf of the Royal Astronomical Society

have also been suggested as the progenitors of quasars (e.g. Sanders et al. 1988b), the central engines of which would be powered by the same gas reservoir that powers their starbursts. Although rare in the local Universe, these objects evolve strongly with redshift even at low redshifts, from $z \sim 0$ to $z \sim 0.3$ (Kim & Sanders 1998). The advent of submm imagers and far-IR space missions subsequent to *IRAS* has shown that higher redshift equivalents of ULIRGs are at least 2 orders of magnitude more common at $z \sim 2$ than they are in the local Universe (e.g. Smail, Ivison & Blain 1997; Hughes et al. 1998; Dole et al. 2001; Gruppioni et al. 2013). Such sources have been implicated in the formation of massive cluster galaxies at high redshift (Farrah et al. 2006), the development of the Cosmic Infrared Background (Dole et al. 2006), and the AGN-triggered quenching of star formation in massive galaxies (Hopkins 2012).

Understanding the physical processes behind the numerous ULIRG-class objects at high redshift is not easy – their distance means they are faint despite their luminosity. This means that we must instead use the local ULIRG population to provide guidance in understanding the more distant objects. Once we understand the local sources, we can then apply this knowledge to the more distant population under the assumption that they are similar enough that local insights can set a baseline for comparison, and detection of any evolution with redshift. ULIRGs are extremely dusty objects, containing typical dust masses of $10^8\,\mathrm{M}_\odot$ or greater. Their most luminous regions can thus be heavily obscured (see e.g. Rangwala et al. 2011). A detailed view of their most obscured regions must thus be obtained at long wavelengths, in the far-IR or submm, since shorter wavelength radiation cannot penetrate the obscuring material. Although there have been a number of studies of individual ULIRGs at these wavelengths in the past (e.g. Fischer et al. 2010; Rangwala et al. 2011; Fischer et al. 2014), it is only through the statistical study of large, complete samples that we will obtain clear insights into the breadth of ULIRG properties and behaviours. This is the role of the *Herschel* ULIRG Survey (HERUS), the largest coherent spectroscopic and photometric survey of local ULIRGs to date.

Previous HERUS papers have largely dealt with the spectroscopic observations of the sample (Pearson et al. 2016; Farrah et al. 2013; Spoon et al. 2013), or results on individual objects, such as IRAS 08572+3915 (Efstathiou et al. 2014). This paper presents the photometric observations of the HERUS ULIRGs obtained using the SPIRE instrument (Griffin et al. 2010) on the *Herschel Space Observatory* (Pilbratt et al. 2010), and results derived from them. These include the results of fitting simple parametric spectral energy distributions (SEDs) to the *IRAS* and HERUS data for these objects and comparing these results to those from similar analysis of other data sets. The simple (T, β) SED model (definition given in Section 5) we use is widely applied in this field (see e.g. Dunne et al. 2000; Clements, Dunne & Eales 2010; Cortese et al. 2014). This model is clearly a major simplification of the emission of actual dust in a real galaxy, since there are many other factors, such as dust at multiple temperatures, optical depth effects (e.g. Rangwala et al. 2011), the evolution of dust properties with time and metallicity, and more that can apply. This can affect the interpretation of such simplified SED fits. Cortese et al. (2014), for example, find that the choice of a fixed β value can strongly affect the derived dust temperature and the correlation of that temperature with other galaxy properties. Fortunately, our current data set provides enough information for β to be a free parameter that is determined during the fitting process, avoiding at least some of these problems. Optical depth effects will tend to flatten the SED around its peak, so that a simple (T, β) model is no longer a good fit, whereas additional dust components, whether warmer or cooler, will also modify the SED and the interpretation of the results. Since ULIRGs are complex and very dusty objects, with strong evidence that at least some are optically thick even at far-IR wavelengths (Rangwala et al. 2011), some of these issues are likely to arise in our data. The physical properties of dust will evolve over time and may well be affected by the strong radiation fields that arise during the massive starbursts and AGN activity that powers a ULIRG. This may be reflected in the results of our SED fits and systematic differences between what we find for ULIRGs and what other authors find for more quiescent galaxies.

The paper is structured as follows: In the next section, we describe the HERUS sample, a complete sample of ULIRGs in the local Universe at $z < 0.3$ and with 60 μm flux >1.8 Jy. In Section 3, we describe the SPIRE observations, and in the subsequent section, we describe the data reduction and photometric results obtained. In Section 5, we use the SPIRE photometry combined with *IRAS* fluxes for these sources to fit a simple parametric dust SED model to the data. From this, we derive ULIRG dust temperatures, emissivities, and masses, and compare these to other far-IR sources in the literature. In Section 6, we look at the residuals to our fits to examine whether there are any systematic issues with our simple model across the whole sample and to see what improvements might be made to this model, compare the far-IR colours of the HERUS ULIRGs to other far-IR samples, and examine the selection effects that might affect the different samples of ULIRG-like objects selected by *IRAS* in the local Universe, and by *Herschel* and/or submm imagers at higher redshift. We summarize our conclusions in Section 7. The SPIRE images of the HERUS ULIRGs and plots of their SED fits are presented in the appendices. We assume a Hubble constant of $H_0 = 70\,\mathrm{km\,s^{-1}\,Mpc^{-1}}$ and density parameters of $\Omega_\mathrm{M} = 0.3$ and $\Omega_\mathrm{L} = 0.7$.

2 THE HERUS SAMPLE

The HERUS (PI D. Farrah, programme ID OT1_dfarrah_1) was, at 250 h, among the largest open time extragalactic programmes carried out by the *Herschel Space Observatory*. It is an unbiased survey of local ULIRGs, comprising a sample of 43 objects selected to be at $z < 0.3$, with 60 μm fluxes >1.8Jy and originally identified in the *IRAS* PSC-z survey (Saunders et al. 2000).

The entire sample was observed by *Herschel* (Pilbratt et al. 2010) using the SPIRE instrument (Griffin et al. 2010) in both photometer mode, at 250, 350, and 500 μm, and in Fourier Transform Spectrometer (FTS) mode. The results of the latter observations are reported in Pearson et al. (2016). The sources were also observed at shorter far-IR wavelengths using the PACS instrument (Poglitsch et al. 2010). These observations were split between the HERUS survey (Spoon et al. 2013; Farrah et al. 2013) and the SHINING survey (Fischer et al. 2010; Sturm et al. 2011; Veilleux et al. 2013; González-Alfonso et al. 2015, 2017; Janssen et al. 2016). Other observations for this sample are also available at a range of resolutions and wavelengths. For more details on the SPIRE spectroscopic observations, see Pearson et al. (2016).

3 SPIRE OBSERVATIONS

The HERUS SPIRE photometry observations were carried out between 2011 August 16 [*Herschel* Operational Day (OD) 825] and 2012 May 16 (OD 1022). The observations are summarized in

Table 1. Summary of HERUS observations of local ULIRGs. The operational day (OD) and observation identification (obsID) are tabulated for the observations made with the SPIRE photometer. Indicative far-IR luminosities ($L_{\rm IR} = L_{8-1000\,\mu{\rm m}}$) calculated following Sanders & Mirabel (1996) are also included for reference.

Target name	Redshift	$\log(L_{\rm IR}/{\rm L}_\odot)$	OD	ObsID
IRAS 00397−1312	0.262	12.97	949	1342234696
Mrk1014	0.163	12.61	976	1342237540
3C273	0.158	12.72	948	1342234882
IRAS 03521+0028	0.152	12.56	1022	1342239850
IRAS 07598+6508	0.148	12.46	862	1342229642
IRAS 10378+1109	0.136	12.38	948	1342234867
IRAS 03158+4227	0.134	12.55	825	1342226656
IRAS 16090−0139	0.134	12.54	862	1342229565
IRAS 20100−4156	0.13	12.63	880	1342230817
IRAS 23253−5415	0.13	12.26	949	1342234737
IRAS 00188−0856	0.128	12.47	949	1342234693
IRAS 12071−0444	0.128	12.31	948	1342234858
IRAS 13451+1232	0.122	12.32	948	1342234792^a
IRAS 01003−2238	0.118	12.25	949	1342234707
IRAS 11095−0238	0.107	12.28	948	1342234863
IRAS 20087−0308	0.106	12.41	880	1342230838
IRAS 23230−6926	0.106	12.32	880	1342230806
IRAS 08311−2459	0.1	12.46	880	1342230796
IRAS 15462−0450	0.099	12.24	989	1342238307
IRAS 06206−6315	0.092	12.23	825	1342226638
IRAS 20414−1651	0.087	12.24	892	1342231345
IRAS 19297−0406	0.086	12.38	880	1342230837
IRAS 14348−1447	0.083	12.33	989	1342238301
IRAS 06035−7102	0.079	12.14	353	1342195728^a
IRAS 22491−1808	0.078	12.18	949	1342234671
IRAS 14378−3651	0.067	12.14	989	1342238295
IRAS 23365+3604	0.064	12.17	948	1342234919
IRAS 19254−7245	0.062	12.06	515	1342206210^a
IRAS 09022−3615	0.06	12.24	880	1342230799
IRAS 08572+3915	0.058	12.16	880	1342230749
IRAS 15250+3609	0.055	12.03	948	1342234775
Mrk463	0.05	11.77	963	1342236151
IRAS 23128−5919	0.045	12.06	544	1342209299^a
IRAS 05189−2524	0.043	12.12	467	1342203632^a
IRAS 10565+2448	0.043	12.08	948	1342234869
IRAS17208−0014	0.043	12.38	467	1342203587^a
IRAS20551−4250	0.043	12.01	880	1342230815
Mrk231	0.042	12.49	209	1342201218^a
UGC5101	0.039	12.01	495	1342204962^a
Mrk273	0.038	12.13	438	1342201217^a
IRAS 13120−5453	0.031	12.22	829	1342226970
NGC6240	0.024	11.93	467	1342203586^a
Arp220	0.018	12.14	229	1342188687^a

^{a}denotes *Herschel* data obtained outside the HERUS project.

Table 1, where the source name, redshift, and IR luminosity ($L_{\rm IR} = L_{8-1000\,\mu{\rm m}}$) are tabulated along with the *Herschel*-SPIRE observation IDs (*obsid*) for the corresponding photometric observations and their OD.

The SPIRE photometer observations were carried out in small map mode (*SpirePhotoSmallScan*, POF10, Dowell et al. 2010) with fixed, three repetition (445s), cross-linked 1 × 1 scan legs, covering a field of 4-arcmin radius. Images are taken simultaneously in the SPIRE 250 µm (*PSW*), 350 µm (*PMW*), and 500 µm (*PLW*) bands. Note that 3C273 only has photometric data, and the photometric data for IRAS 06035−7102 was extracted from the Open Time Key Programme: KPOT_mmeixner observations of the Large Magellanic Cloud, Level 2.5 *Herschel* data product.

4 DATA REDUCTION AND RESULTS

All SPIRE photometry observations (listed in Table 1) were processed through the standard Small Map User Pipeline with HIPE 11.2825, using SPIRE Calibration Tree 11.0 with default values for all pipeline tasks. Target positions in the map were found by the HIPE SUSSEXtractor task (Savage & Oliver 2007), assuming a full width at half-maximum (FWHM) of 18.15, 25.2, and 36.9 arcsec for the *PSW*, *PMW*, and *PLW* bands, respectively. These positions were then input into the SPIRE Timeline Fitter task within the HIPE environment (Pearson et al. 2014) that fits a Gaussian function to the baseline-subtracted SPIRE timelines. The background is measured within an annulus of between 300 and 350 arcsec, and then an elliptical Gaussian function is fit to both the central 22, 32, and

Table 2. Photometry of the HERUS galaxies in the SPIRE bands *PSW* (250 µm), *PMW* (350 µm), *PLW* (500 µm). These fluxes originally appeared in Pearson et al. (2016).

Target	*F250*		*F350*		*F500*	
	Flux density Jy	Error Jy	Flux density Jy	Error Jy	Flux density Jy	Error Jy
IRAS 00397−1312	0.389	0.004	0.130	0.004	0.040	0.005
Mrk1014	0.460	0.004	0.175	0.004	0.063	0.005
3C273	0.437	0.004	0.633	0.004	0.994	0.005
IRAS 03521+0028	0.684	0.004	0.270	0.004	0.094	0.004
IRAS 07598+6508	0.500	0.004	0.197	0.004	0.058	0.005
IRAS 10378+1109	0.480	0.004	0.183	0.004	0.050	0.005
IRAS 03158+4227	0.973	0.004	0.377	0.004	0.137	0.005
IRAS 16090−0139	1.067	0.004	0.404	0.004	0.116	0.005
IRAS 20100−4156	1.001	0.004	0.349	0.004	0.102	0.005
IRAS 23253−5415	1.044	0.005	0.437	0.004	0.165	0.005
IRAS 00188−0856	0.877	0.004	0.345	0.004	0.111	0.005
IRAS 12071−0444	0.471	0.004	0.163	0.004	0.044	0.005
IRAS 13451+1232	0.503	0.005	0.256	0.004	0.197	0.006
IRAS 01003−2238	0.222	0.004	0.070	0.004	0.026	0.006
IRAS 23230−6926	0.617	0.004	0.204	0.004	0.064	0.005
IRAS 11095−0238	0.380	0.004	0.119	0.004	0.036	0.005
IRAS 20087−0308	1.804	0.006	0.687	0.004	0.210	0.005
IRAS 15462−0450	0.492	0.004	0.162	0.004	0.050	0.008
IRAS 08311−2459	1.246	0.005	0.464	0.004	0.148	0.005
IRAS 06206−6315	1.248	0.005	0.477	0.004	0.158	0.005
IRAS 20414−1651	1.315	0.005	0.519	0.004	0.168	0.005
IRAS 19297−0406	2.039	0.006	0.752	0.004	0.244	0.005
IRAS 14348−1447	1.842	0.006	0.666	0.005	0.197	0.006
IRAS 06035−7102	1.226	0.022	0.397	0.001	0.130	0.008
IRAS 22491−1808	0.862	0.004	0.305	0.004	0.097	0.005
IRAS 14378−3651	1.330	0.005	0.478	0.005	0.135	0.006
IRAS 23365+3604	1.849	0.006	0.669	0.004	0.210	0.005
IRAS 19254−7245	1.545	0.005	0.587	0.004	0.185	0.005
IRAS 09022−3615	2.449	0.007	0.823	0.004	0.252	0.005
IRAS 08572+3915	0.504	0.004	0.164	0.004	0.060	0.004
IRAS 15250+3609	0.966	0.004	0.368	0.004	0.136	0.005
Mrk463	0.344	0.004	0.134	0.004	0.052	0.005
IRAS 23128−5919	1.565	0.008	0.556	0.006	0.176	0.007
IRAS 10565+2448	3.619	0.011	1.319	0.004	0.407	0.005
IRAS 20551−4250	1.629	0.005	0.556	0.004	0.170	0.005
IRAS 05189−2524	1.963	0.011	0.717	0.007	0.211	0.009
IRAS 17208−0014	7.918	0.037	2.953	0.010	0.954	0.009
Mrk231	5.618	0.019	2.011	0.008	0.615	0.008
UGC5101	6.071	0.039	2.327	0.018	0.746	0.009
Mrk273	4.190	0.011	1.493	0.006	0.471	0.006
IRAS 13120−5453	12.097	0.036	4.441	0.010	1.355	0.006
NGC6240	5.166	0.029	2.031	0.009	0.744	0.008
Arp220	30.414	0.132	12.064	0.036	4.145	0.015

40 arcsec (for the *PSW*, *PMW*, and *PLW* bands, respectively) and the background annulus. The results for the photometry of all the HERUS galaxies is shown in Table 2, whereas the images in the three *Herschel* bands are included in Appendix A. Absolute flux calibration accuracy for SPIRE is estimated to be 4 per cent, whereas relative flux errors are 1.5 per cent or better (Bendo et al. 2013).

A small number of sources appear to have close companions in the SPIRE images. These include IRAS 01003−2238 (80 arcsec separation), IRAS14378−3651 (30 arcsec separation), IRAS15462−0450 (35 arcsec separation), and IRAS23253−5415 (27 arcsec separation). In most cases, the companions are detected in 2MASS with comparable magnitudes and usually somewhat bluer colours than the ULIRG itself. The conclusion of Duc, Mirabel & Maza (1997) that the main component in IRAS15462−0450, which they classify as a loose interacting pair, is responsible for all the *IRAS* emission is perhaps challenged by the HERUS SPIRE images, which show that the component about 35 arcsec to the S might contribute about 20 per cent of the flux. In contrast to the others, the companion ∼27 arcsec to the NE of IRAS23253−5415 is not detected by 2MASS, but it is detected by the *Wide-field Infrared Survey Explorer* (*WISE*). The *WISE* images suggest that this companion and a weaker extension to the E may, in fact, all be part of the same system. A detailed analysis of the companions and a search for any weak extended far-IR emission in these systems, which are largely unresolved by SPIRE, is beyond the scope of this paper.

5 DUST PROPERTIES OF THE HERUS ULIRGS

The far-IR properties of galaxies can be studied by fits of their far-IR to submm SEDs to models of various types. These can range

Table 3. Comparison samples used in this study. Basic selection criteria are given but some more complex aspects, such as low galactic foreground, omitted for clarity. See the relevant papers for full details. The complete column indicates whether the sample can be considered statistically complete. LTG = late type galaxies, ETG = early type galaxies. The HATLAS DR1 region amounts to 161 deg^2 in three equatorial regions (Eales et al. 2010). *two higher z lensed sources also included. The HerMES region amounts to 90 deg^2 in a number of fields (Oliver et al. 2012). See Chapman et al. (2005) for details of the regions surveyed. Redshift range for these sources is 0.08–3.4. Fixed in the β column indicates that this parameter was set to this value and not part of the fit.

Source	Selection	Complete?	Passbands used (μm)	$\bar{T}$ (K)	$\bar{\beta}$
Current Work	ULIRGs, $z < 0.3$, $F_{60} > 1.8$Jy	Yes	60, 100, 250, 350, 500	37.9	1.8
Cortese et al. (2014)	$15 < D < 25$Mpc, $K < 12.5$ LTG, $K < 8.7$ ETG	Yes	100, 160, 250, 350, 500	21.3	1.7
Clements et al. (2010)	ULIRGs, $F_{60} > 1$ Jy, 850 μm detected ($z < 0.19$)	No	60, 100, 850	42	1.6
Dunne et al. (2000)	$\nu > 1900\,\mathrm{km\,s^{-1}}$ $F_{60} > 5.4$ Jy $-10 < \delta < 50$	Yes	60, 100, 850	35.6	1.3
Smith et al. (2013)	$z < 0.5$ HATLAS DR1 region, $F_{250} > 20.4$ mJy	Yes	100, 160, 250, 350, 500	23.5	1.82
Magdis et al. (2014)	$0.22 < z < 0.9*$, $F_{250} > 150$mJy, HerMES region	Yes	70, 160, 250, 350, 500	36	1.5 fixed
Chapman et al. (2005)	$F_{850} > 4.5$ mJy, SCUBA surveys$^+$, 1.4 GHz detected	No	850, 1.4 GHz	36	1.5 fixed
Yang et al. (2007)	$F_{60} > 0.2$Jy, z known ($0.1 < z < 1$), K known	No	60, 100, 350, 1.4 GHz	42.8	1.5 fixed
Huang et al. (2014)	$z > 4$, 250 and 350 detected	No	250, 350, 850, 1100	64	2.0 fixed

from simple parametrized models of modified black bodies (e.g. Clements, Andreani & Chase 1993; Dunne et al. 2000; Bendo et al. 2003; Vlahakis, Dunne & Eales 2005; Clements et al. 2010; Cortese et al. 2014; , and references therein) to multicomponent dust models (e.g. Dunne & Eales 2001; Klaas et al. 2001; Clements et al. 2010), to full-scale radiative transfer models that include dust of different compositions at a wide range of temperatures (e.g. Farrah et al. 2003; Ciesla et al. 2014; Efstathiou & Siebenmorgen 2009). Needless to say, the more complex the model, the more photometric points over a wider range of wavelengths are needed to properly constrain the fit. For the present photometric atlas, which includes just the combination of *IRAS* and SPIRE photometry from 60 to 500 μm that is available for the complete data set, we restrict ourselves to the simplest of the parametric models available, a modified blackbody function where the emission as a function of frequency, ν, is given by

$$F_\nu[\nu, T, \beta] \propto \nu^\beta B_\nu(\nu, T), \tag{1}$$

where F_ν is the flux density in Jy, β is an emissivity parameter that typically has a value between 1 and 2, T is a parameter specifying the dust temperature, and $B_\nu(\nu, T)$ is the standard blackbody function. We do not claim that the dust SED in the HERUS ULIRGs, or in fact any galaxy, is explained by dust of a single type at a single temperature, we simply use this particular commonly used SED parametrization as a way of comparing the far-IR properties of the HERUS ULIRGs to those of other galaxy samples that have widely been fitted using a similar parametrization. Future papers (Farrah et al., in preparation, Clements et al., in preparation, Efstathiou et al., in preparation) will explore other types of SED fits using a wider range of heterogenous data, including the off-line continuum fluxes from our PACS observations, as well as a range of more sophisticated parametric and physical models.

Once we have fitted the SEDs of our HERUS sources to this model, we compare our results to those of a number of different studies of both ULIRGs and other galaxy samples in the literature. In Table 3, we list these samples, their selection criteria, the basic parameters of the observations, and statistics of their results as well as similar details for the current work.

Two of our sources, 3C273 and IRAS 13451+1232 (aka 4C12.5), are dominated by non-thermal emission in the far-IR (Clements et al. 2010). Analysis of the properties of any dust emission in these objects thus requires a thorough knowledge of the non-thermal synchrotron spectrum in these sources, which is beyond the scope of this paper. We thus exclude these objects from further consideration here.

5.1 Fitting method

We adopt a Bayesian fitting method for the HERUS sources similar to that used for nearby galaxies observed by Planck (Planck Collaboration XVI 2011). We start with a model of the data where the measured flux d_ν at frequency ν is of the form as follows:

$$d_\nu = A F_\nu\,[(1+z)\nu; T, \beta] + n_\nu, \tag{2}$$

where A gives the overall amplitude of the SED and $(1 + z)$ converts the rest-frame frequency to the observed frequency of a given channel for an object at a redshift of z. The noise contribution at a given frequency ν is given by n_ν, which we model as a Gaussian with variance σ_ν^2 and which is determined by the *Herschel* or *IRAS* observations. The parameters of our model are thus A, β, and T. We fit these to the data for each individual HERUS ULIRG, using the EMCEE Markov chain Monte Carlo package[1] (Foreman-Mackey et al. 2013, for the general approach, see also Lewis & Bridle 2002; Jaynes 2003) to probe the parameter space, equivalent to an exploration of the χ^2 surface with a non-linear parametrization. We apply the following priors for our parameter values: For temperature (T), we adopt a uniform prior between 3 and 100K, for emissivity (β), we adopt a uniform prior between 0 and 3, and for A, because the wide range of distances for our sources implies a range of amplitudes covering several orders of magnitude, we adopt a uniform prior on log (A) between −3 and 10. The probability is zero outside the range of these uniform prior distributions.

We start a series of MCMC chains at positions in the three parameter search space chosen at random from a uniform distribution with $T = 30$–50 K, $\beta = 1.2$–1.8, and $\log(A) = -1$ to 3 to match our expectation for the likely range of these parameters. A hundred of these starting points were chosen and the MCMC engine was then used to generate 600 further steps along each of these chains for a total of 60 000 samples. The first 100 steps in each of these chains are regarded as ‘burn-in time’ and the remaining 50 000 samples are used to determine the best-fitting parameters and their posterior distributions. Figs 1 and 2 show the sampling chain, the resulting two dimensional and marginalized likelihood functions, and the resulting SED fit for IRAS 00397−1312 to demonstrate this fitting

---

[1] http://dan.iel.fm/emcee/current/

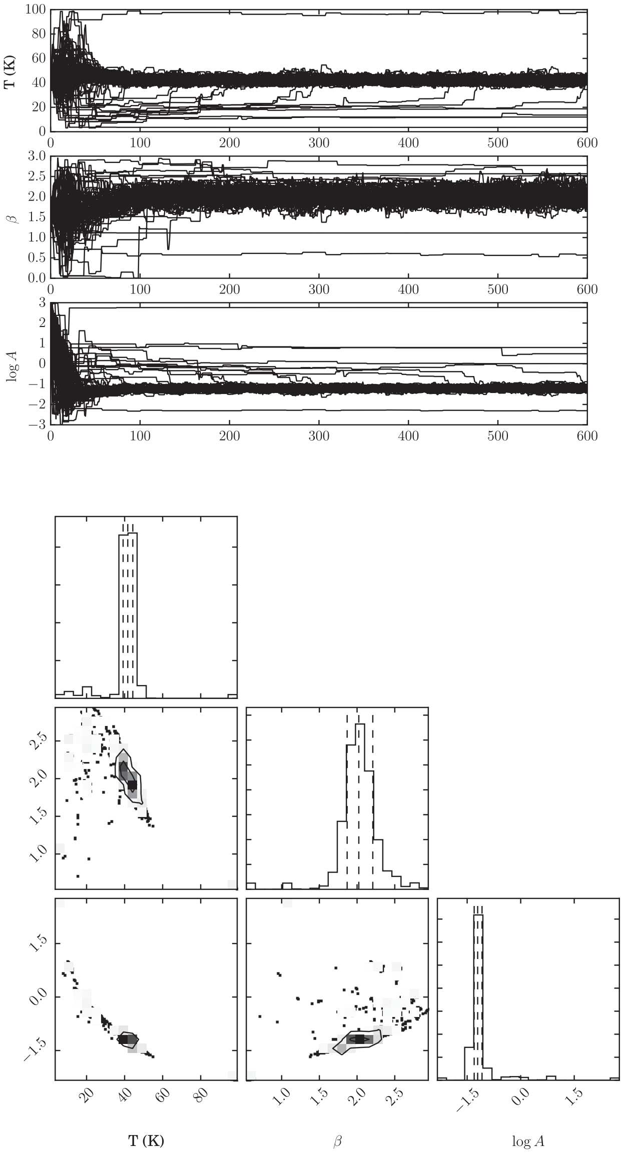

Figure 1. Demonstration of our MCMC fitting method as applied to the ULIRG IRAS 00397−1312. Top panel: The complete set of 100 MCMC chains, including the first 100 steps of burn-in period, which are discarded. The convergence of nearly all the chains to very similar values demonstrates the reliability of the fitting process. Bottom panel: The two dimensional and marginalized posterior likelihood functions showing that the SED parameters are very well fitted by this method.

process. The results of these fits, giving the median in the marginalized posterior distributions as the fitted value and the 32nd and 68th percentiles of the distribution as the 1σ errors, are given in Table 4.

One potential issue with our fitting method is that several of our main comparison samples use data from a different range of filters: We use IRAS+SPIRE at 60, 100, 250, 350, and 500 µm, whereas the wholly *Herschel* derived samples use PACS+SPIRE at 100, 160, 250, 350, and 500 µm. We tested whether these differences might introduce biases into our results by taking a range of model SEDs of known temperature, extracting model fluxes at the relevant wavelengths, adding noise appropriate to the different sets of observations, and then seeing whether there were any significant deviations from a one-to-one fit. The only significant issue we find is a bias towards higher dust temperatures for fits using PACS+SPIRE data for input dust temperatures >50K, where the output temperature is high compared to that input. There were no substantial biases for the IRAS+SPIRE models comparable to the HERUS data. Since there are no PACS+SPIRE sources with $T > 50K$ in our comparison samples, we conclude that no significant biases are introduced to our analysis as a result of the slightly different wavelength bands being used.

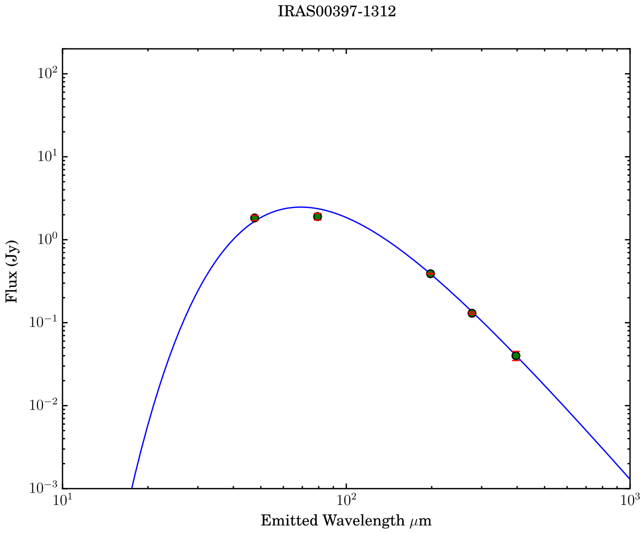

Figure 2. The final fitted SED for IRAS00397−1312 using the median set of marginalized parameters derived from the MCMC fitting process. Fit is shown as the blue line, and data points as green dots. Error bars on the fluxes are also shown (in red) but are generally smaller than the green dots of the data points.

5.2 Fit results

Plots of the fitted SEDs compared to the observational data can be found in Appendix B. The distribution of temperature and β values derived from these fits is shown in Figs 3 and 4, where they are also compared to similar results from the Herschel reference sample (HRS) Survey (Cortese et al. 2014). The ULIRGs clearly have warmer temperatures than the lower luminosity HRS sources (median temperatures of 37.9K, standard deviation 4.7K for the ULIRGs compared to 21.3K with a standard deviation of 3.4K for the HRS sources). They also have very similar median β values (medians of 1.7 and 1.8, respectively), though the HRS sources have a wider range of β values.

Comparing our results with previous ULIRG SED studies, such as Clements et al. (2010), which are based on IRAS data combined with submm photometry at 850 µm, and in some cases 450 µm, shows broad agreement between the fits, with typical differences of less than 5K between the SPIRE and submm derived temperatures. Deriving population averages from such samples, though, is difficult since previous work is largely based on incomplete samples with non-detections at submm for many of the fainter objects. The SPIRE derived temperatures are usually lower than the submm temperatures. There are three outliers where there is a large difference in derived temperature, with $T_{\rm SPIRE} - T_{\rm submm} > -10$K. One of these (IRAS08572+3915), which has the largest temperature discrepancy in the fitting ($T_{\rm SPIRE} - T_{\rm submm} = -12.5$ K), had only a very low significance 850-µm detection (2.7σ) so we might expect its submm SED fit to be unreliable. IRAS 10378+1108, with $T_{\rm SPIRE} - T_{\rm submm} = -11$ K, has a 4σ 850-µm detection which, while

Table 4. Results of single component parametric fits to the dust SEDs of HERUS ULIRGs. T+ and T− represent the 68 per cent confidence interval on the marginalized MCMC fit to the temperature parameter and similarly for B+, B− and A+ and A− for the β and $\log A$ parameters, respectively. The $\log A$ parameter is arbitrarily normalized.

Name	z	Temp (K)	T+	T-	Beta	B+	B-	A	A+	A-	Dust Mass ($log\,M_{\odot}$)
Arp220	0.018	35.51	0.25	0.26	1.58	0.01	0.01	0.93	0.01	0.01	8.3
NGC6240	0.024	41.36	0.18	0.16	1.41	0.01	0.01	−0.04	0.01	0.01	7.7
IRAS 13120−5453	0.031	36.78	0.07	0.07	1.64	0.01	0.00	0.48	0.01	0.01	8.4
Mrk273	0.038	36.34	0.32	0.33	1.89	0.01	0.01	0.15	0.01	0.01	8.1
UGC5101	0.039	34.47	0.16	0.14	1.51	0.01	0.02	0.17	0.01	0.01	8.4
Mrk231	0.042	36.87	0.41	0.43	1.89	0.02	0.02	0.26	0.02	0.02	8.3
IRAS 05189−2524	0.043	46.73	0.29	0.28	1.44	0.01	0.02	−0.58	0.01	0.01	7.7
IRAS 20551−4250	0.043	45.43	0.21	0.20	1.58	0.01	0.01	−0.58	0.01	0.01	7.6
IRAS 17208−0014	0.043	38.12	0.20	0.18	1.66	0.01	0.01	0.28	0.01	0.01	8.5
IRAS 10565+2448	0.043	36.60	0.12	0.11	1.67	0.01	0.01	−0.03	0.01	0.01	8.2
IRAS 23128−5919	0.045	42.25	0.32	0.31	1.72	0.02	0.02	−0.48	0.01	0.01	7.7
Mrk463	0.05	43.39	3.84	4.28	1.46	0.15	0.11	−1.26	0.14	0.11	7.2
IRAS 08572+3915	0.058	51.45	1.20	1.10	1.75	0.05	0.05	−1.13	0.03	0.04	7.3
IRAS 15250+3609	0.058	47.67	1.06	0.97	1.45	0.03	0.04	−0.90	0.03	0.03	7.7
IRAS 09022−3615	0.06	35.38	0.16	0.15	2.06	0.01	0.01	−0.03	0.01	0.01	8.3
IRAS 19254−7245	0.062	35.97	0.24	0.24	1.76	0.02	0.02	−0.35	0.01	0.01	8.2
IRAS 23365+3604	0.064	36.49	0.19	0.20	1.85	0.02	0.02	−0.26	0.01	0.01	8.2
IRAS 14378−3651	0.067	37.89	0.35	0.35	1.89	0.03	0.03	−0.42	0.02	0.02	8.1
IRAS 22491−1808	0.078	54.63	0.32	0.35	1.11	0.01	0.01	−1.22	0.01	0.01	7.8
IRAS 06035−7102	0.079	36.91	0.69	0.71	1.94	0.05	0.06	−0.46	0.04	0.04	8.2
IRAS 14348−1447	0.083	37.63	0.21	0.21	1.71	0.02	0.02	−0.36	0.01	0.01	8.5
IRAS 19297−0406	0.086	36.39	0.23	0.21	1.84	0.02	0.02	−0.24	0.01	0.01	8.6
IRAS 20414−1651	0.087	37.34	0.58	0.66	1.65	0.03	0.03	−0.52	0.03	0.02	8.4
IRAS 06206−6315	0.092	36.72	0.37	0.39	1.72	0.03	0.03	−0.51	0.02	0.02	8.4
IRAS 08311−2459	0.099	37.41	0.67	0.73	1.81	0.03	0.03	−0.50	0.03	0.03	8.5
IRAS 15462−0450	0.1	33.60	0.99	1.07	2.28	0.09	0.09	−0.63	0.07	0.06	8.1
IRAS 11095−0238	0.106	41.15	1.31	1.37	2.08	0.08	0.08	−1.01	0.06	0.06	7.9
IRAS 20087−0308	0.106	34.11	0.43	0.49	1.88	0.03	0.02	−0.24	0.02	0.02	8.8
IRAS 23230−6926	0.107	39.11	0.77	0.74	1.99	0.05	0.05	−0.79	0.04	0.04	8.2
IRAS 01003−2238	0.118	45.30	2.48	2.37	1.96	0.13	0.13	−1.38	0.09	0.09	7.7
IRAS 12071−0444	0.128	38.57	1.00	1.03	1.99	0.07	0.07	−0.92	0.05	0.05	8.3
IRAS 00188−0856	0.128	35.76	0.88	1.05	1.74	0.05	0.05	−0.67	0.05	0.04	8.6
IRAS 20100−4156	0.13	39.51	0.40	0.39	1.96	0.03	0.03	−0.63	0.02	0.02	8.6
IRAS 23253−5415	0.13	37.67	0.67	0.72	1.46	0.03	0.03	−0.74	0.03	0.03	8.7
IRAS 03158+4227	0.134	42.30	1.26	1.37	1.58	0.04	0.04	−0.84	0.04	0.04	8.6
IRAS 16090−0139	0.134	37.50	0.43	0.44	1.84	0.03	0.03	−0.60	0.02	0.02	8.7
IRAS 10378+1109	0.136	42.04	1.06	1.08	1.61	0.06	0.06	−1.13	0.04	0.04	8.3
IRAS 07598+6508	0.148	40.34	0.83	0.81	1.60	0.05	0.05	−1.09	0.04	0.04	8.5
IRAS 03521+0028	0.152	42.62	1.15	1.27	1.57	0.05	0.05	−1.02	0.04	0.04	8.6
Mrk1014	0.163	46.89	1.10	1.14	1.50	0.07	0.06	−1.30	0.04	0.04	8.4
IRAS 00397−1312	0.262	41.73	1.19	1.19	2.03	0.08	0.08	−1.21	0.05	0.05	8.9

comparatively low, was not unusual in the Clements et al. (2010) data set. The final discrepant object, with $T_{\rm SPIRE} - T_{\rm submm} = -10.5$K, is Arp220, which is strongly detected in all bands. Rangwala et al. (2011) used a wider range of photometric data to show that Arp220 is optically thick to 235 μm, which is likely the origin of the discrepancy.

5.3 Temperature–β Relation

The relation between dust temperature and β is shown in Fig. 5, which also shows similar data for the HRS from Cortese et al. (2014). As can be seen, the HRS sources and the HERUS ULIRGs both show an anticorrelation between T and β, with hotter sources having a shallower β. The correlation coefficient for the HERUS sources is -0.51 with a probability of this arising at random of 0.000 62. However, the relationships are quite different. The gradient of the anticorrelation is significantly shallower for ULIRGs, and there is a clear offset in temperature of about +15K between the HERUS and HRS samples. The temperature offset might simply come from increased dust heating in the higher luminosities of ULIRGs relative to the HRS galaxies, or possibly result from an AGN contribution to the luminosity, but the different relationship to β is more interesting. Cortese et al. (2014) find a correlation between β and metallicity with lower metallicity systems having a systematically lower β value. Temperature, in contrast, was found to be mainly related to specific star formation rate. Pereira-Santaella et al. (2017) have recently suggested that ULIRGs may be low metallicity systems for their high stellar mass on the basis of far-IR spectroscopy. The range of β values seen here for ULIRGs, 1.5 to 2, would, when compared to the HRS sample, imply a fairly typical HRS metallicity of $12 + \log O/H \sim 8.5 - 8.7$. This is consistent with the metallicities of $8.5 < 12 + \log O/H < 8.9$ inferred by Pereira-Santaella et al. (2017). The higher temperatures seen in ULIRGs for these β values would then be due to the higher

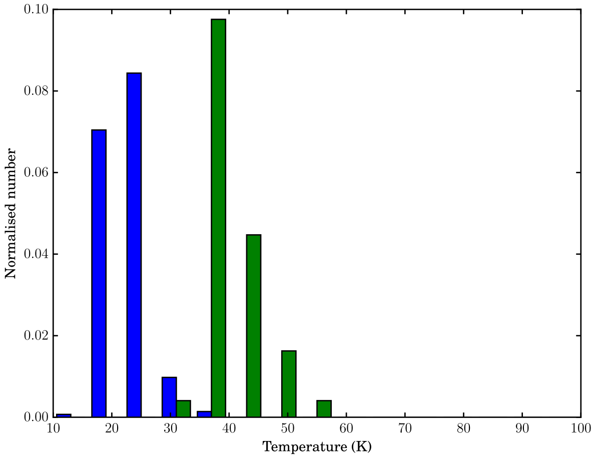

Figure 3. Histogram of the SED fit temperature parameter from the HERUS ULIRG sources (green) compared to similar results form the lower luminosity HRS galaxies (blue, Cortese et al. 2014).

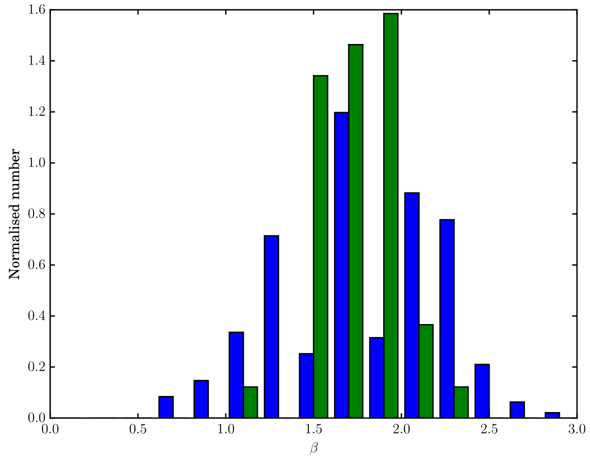

Figure 4. Histogram of the SED fit β parameter from the HERUS ULIRG sources (green) compared to similar results form the lower luminosity HRS galaxies (blue, Cortese et al. 2014).

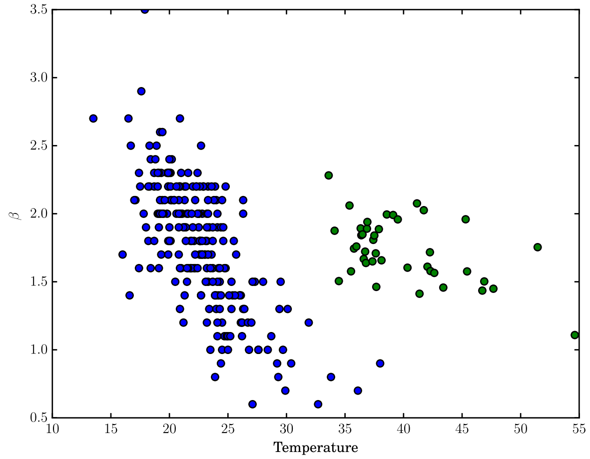

Figure 5. The temperature–β correlation for HERUS ULIRGs (green) and HRS galaxies (blue).

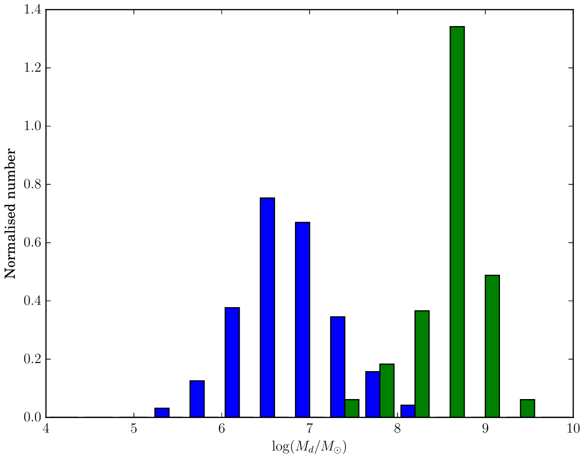

Figure 6. Histogram of dust masses derived from our SED fits to the HERUS ULIRGs (green) compared to similar results form the lower luminosity HRS galaxies (blue, Cortese et al. 2014).

specific star formation rate in these systems. Alternatively, the anticorrelation may reflect differences in the optical properties of the dust as it evolves. Two studies in our own galaxy (Köhler, Ysard & Jones 2015; Ysard et al. 2015) show that variations in the dust optical properties due to coagulation are able to reproduce the observed variations in T and β from the diffuse to the dense interstellar medium.

5.4 Dust masses

We follow Cortese et al. (2014) in calculating an estimate of the dust mass in these objects using the equation

$$F_\nu = \frac{M_{\rm Dust}}{D^2}\kappa_{\nu_0}\left(\frac{\nu}{\nu_0}\right)^{\beta} B_\nu(T), \tag{3}$$

where F_ν, T, β, and B_ν have previously been defined, D is the luminosity distance of the source, $M_{\rm Dust}$ is the dust mass, and we take ν_0 to be 856.5 GHz (ie. 350 µm) and κ_{ν_0} to be 0.192 $\rm m^2\ kg^{-1}$ (Draine 2003). The resulting HERUS ULIRG dust masses, and a comparison to the HRS dust masses from Cortese et al. (2014), are shown in Fig. 6. The HERUS ULIRGs are found to have significantly larger dust masses than the HRS sources, with a median dust mass of $10^{8.3}\ {\rm M}_\odot$, with standard deviation of $10^{0.4}\ {\rm M}_\odot$, compared to the HRS median of $10^{6.8}\ {\rm M}_\odot$, with standard deviation of $10^{0.5}\ {\rm M}_\odot$. If one considers that ULIRGs are likely the result of a merger of two galaxies and divide their dust mass by 2, giving a median progenitor dust mass of $10^{8.0}\ {\rm M}_\odot$, this is still over a factor of 10 greater dust mass than is seen in the HRS population, and comparable to the most dust rich sources in either the HRS or in the IR-selected samples of nearby galaxies in Dunne et al. (2000) and Vlahakis et al. (2005). The stellar masses of HRS sources cover a wide range, ($8 \leq \log M_*/{\rm M}_\odot \leq 12$). Determining the stellar mass of ULIRGs is complicated by the range of obscurations in these systems and by contributions from AGN to the optical/NIR SED. Nevertheless, Hou et al. (2011) used the stellar population fitting code STARLIGHT to derive stellar masses for a sample of 160 ULIRGs selected from SDSS. They found that ULIRG stellar masses range is 10^{10}–$10^{12}\ {\rm M}_\odot$, with AGN dominated ULIRGs having the highest masses. This places them at the upper range of stellar masses in HRS. The progenitors of ULIRGs must thus be either very massive systems or be among the most dust rich, and thus gas rich, members of the field galaxy population, unless there is significant dust

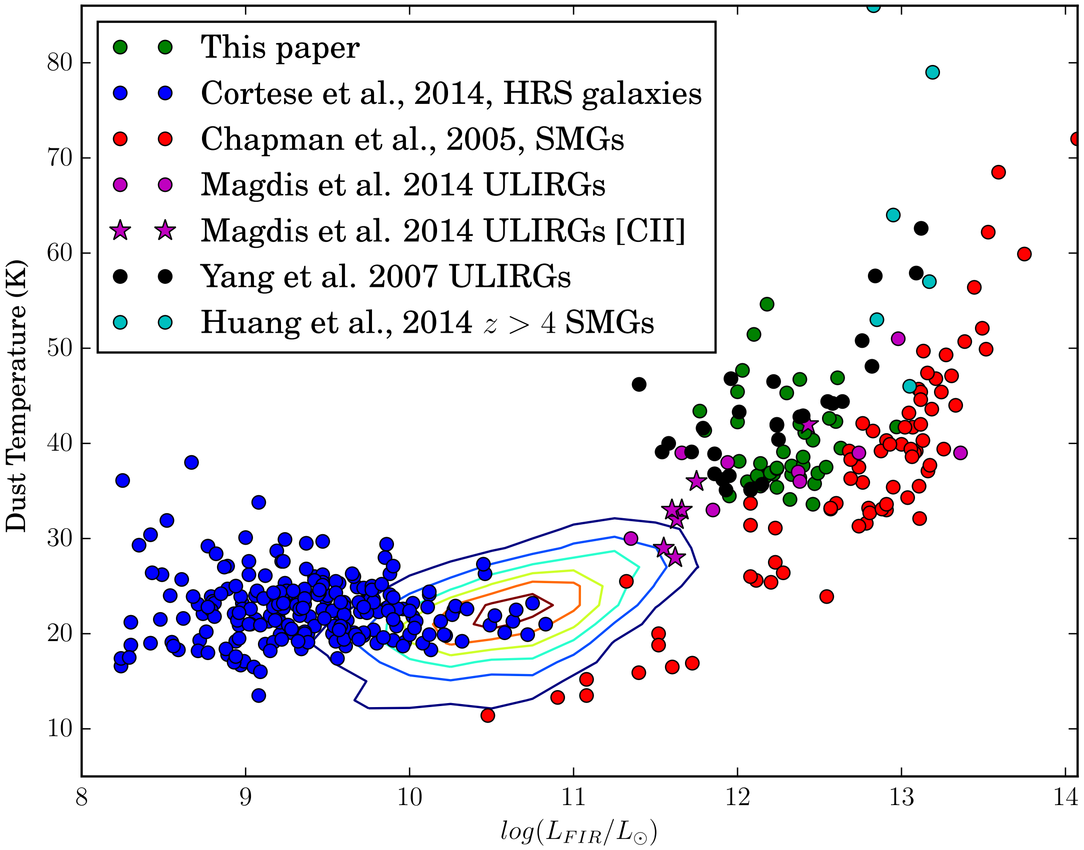

Figure 7. The FIR luminosity–temperature plane for the HERUS ULIRGs and other samples from the literature. HERUS ULIRGs are shown as green dots, whereas sources from the HRS (Cortese et al. 2014) are shown in blue, SMGs from Chapman et al. (2005) are shown in red, intermediate redshift ULIRGs from Yang et al. (2007) are shown in black and Magdis et al. (2014) shown in magenta (those sources with [C II] observations are shown as stars, the others as dots), whereas $z > 4$ SMGs from Huang et al. (2014) are shown in cyan. The contours indicate the distribution of 13826 H-ATLAS 250 µm selected sources from Smith et al. (2013).

production in the early stages of the evolution of a merger into a ULIRG.

5.5 Temperature–Luminosity Diagram

In Fig. 7, we plot the positions of the HERUS ULIRGs in the luminosity–temperature plane alongside various comparison samples from the literature. The latter include local galaxies from the HRS (Cortese et al. 2014), SMGs from Chapman et al. (2005), intermediate redshift ULIRGs from Yang et al. (2007) and Magdis et al. (2014), and $z > 4$ SMGs from Huang et al. (2014). We also plot the population of H-ATLAS 250-µm selected galaxies from Smith et al. (2013) as contours (sources selected to be detected at $>5\sigma$ at 250 µm, with optical counterparts and spectroscopic redshifts largely from SDSS (Abazajian et al. 2009) or GAMA (Driver et al. 2011) and with $z < 0.5$; see the Smith et al. paper for details). Most of these works are applying a single temperature T–β fitting approach to the data similar to that applied here, so we are comparing like-with-like in this plot.

Previous realizations of this plot, with smaller data sets, poorer coverage of the far-IR SED (e.g. Clements et al. 2010), and, in at least some cases, with different assumptions about the dust SED (e.g. fixed rather than variable β values) suggested that high redshift sources such as those of Chapman et al. (2005), lying at $z \sim 2$, or those of Huang et al. (2014), lying at $z > 4$, occupied part of this diagram largely disjoint from more local high $L_{\rm FIR}$ sources, with the SMGs having lower temperatures than nearby ULIRGs. The current data sets still show this to some extent, but the gap between the SMGs and more local ULIRGs is being filled, largely by sources from HERUS and Magdis et al. (2014). The highest redshift SMGs in this plot, from Huang et al. (2014), also appear rather warmer than the lower redshift SMGs of Chapman et al. This suggests that the earlier distinction between the two populations was likely a result of sample incompleteness, with earlier observations failing to cover cooler local ULIRGs or warmer high z SMGs. There is also the possibility that the different selection methods used for these sources – 60 µm flux for *IRAS*-based samples like HERUS, 250 µm flux for the *Herschel*-based samples such as Magdis et al., and 850-µm flux for the SMGs of Chapman et al. and Huang et al. – might have an effect. This is a possibility we explore in more detail later in this paper.

6 DISCUSSION

6.1 What are the real Dust SEDs of ULIRGs?

Although we have fitted a parametrized single (T, β) model to the SEDs of the HERUS galaxies, it is far from certain that this simple model is adequate for fitting the data. A single temperature and β value for all of the dust in a galaxy is almost certainly an over simplification, especially since physical dust properties are likely to evolve differently in different environments in the same galaxy (see

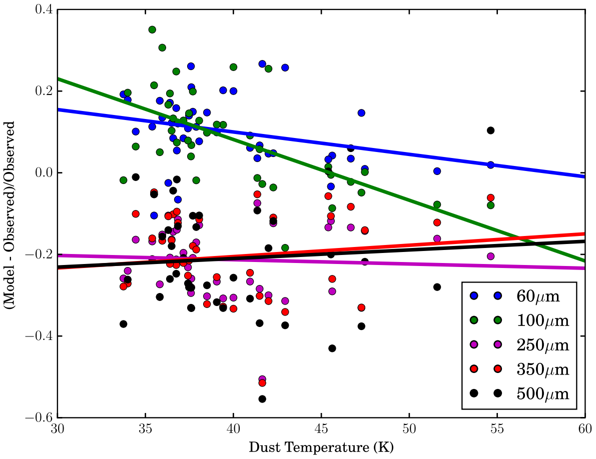

Figure 8. Flux residuals, (model flux − observed flux)/observed flux, for the 60, 100, 250, 350, and 500 μm bands (blue, green, magenta, red, black, respectively) plotted against fitted dust temperature. The solid lines are straight line fits to the data at the matching wavelength. Correlations between residual flux and fitted temperature are only found for the 60 and 100 μm channels, of which the 100 μm correlation is by far the strongest.

e.g. Köhler et al. 2015). Our current investigation uses only the five photometric points from *Herschel* and *IRAS*. More complex models can be fitted to those sources where more data is available – an example for this can be found for Arp220 in Rangwala et al. (2011). Such an analysis will be the subject of a future HERUS paper, but these additional photometric data are inhomogeneously distributed, with some HERUS sources being very well studied, whereas others have little more data than is presented here. Conclusions from such a study might thus be biased in some statistical sense towards, for example, brighter or more nearby ULIRGs. The use of a simple model that can be applied uniformly to a larger data set, as done here, can thus have substantial value.

We can gain insights into the appropriateness of our simple parametric SED model by searching for trends in the flux residuals between our fits and the real data. We plot the relative residuals, $(F_{\rm model} - F_{\rm obs})/F_{\rm obs}$, against model dust temperature in Fig. 8.

The SPIRE and *IRAS* data behave quite differently. The model generally underpredicts SPIRE fluxes by about 20 per cent, but there is no correlation between the residual and the modelled dust temperature – the results of fitting a straight line to the data finds correlation coefficients of −0.06, 0.13, and 0.07 with the probability of there being no correlation of 0.72, 0.43, and 0.65 for the 250, 350, and 500 μm channels, respectively. In contrast, the model usually overpredicts the 60 and 100 μm fluxes, and the size of this residual, ranging from 0 to about 25 per cent, is correlated with model dust temperature. This effect is most apparent at 100 μm and can be seen in many of the SED fits plotted in Appendix B. The correlation coefficients are −0.3 and −0.6, and the chances of this arising at random are 0.05 and 2×10^{-5} at 60 and 100 μm, respectively. A correlation between temperature and residual is thus clearly present at 100 μm and marginally so at 60 μm, but completely absent in the *Herschel* bands.

This result suggests that the real SEDs of ULIRGs may be different to the simple parametric model used here. This is not a surprise in itself since there are several ways in which the SED of a genuine object is likely to differ from a single temperature parametrization. These include the presence of dust components at other temperatures, whether cooler than the temperature found in our single *T* fits (e.g. Clements et al. 2010; Dunne & Eales 2001), the contamination of the 60 μm band by significantly warmer dust (e.g. Mrk231 and Mrk273), or a flattening of the 60-to-250 μm SED as a result of the dust being optically think at these wavelengths, as has been found for Arp220 by Rangwala et al. (2011). A full analysis of these possibilities would require more data points than the five we have for the complete HERUS sample. However, we may gain some insight into these more complex models by seeing if the amplitude of the residuals and the correlation with temperature can be reproduced by simple toy models of more complicated dust SEDs.

We explore three different possibilities: (i) hot dust contamination at short wavelengths, (ii) cold dust contribution rising to longer wavelengths, and (iii) dust that is optically thick at far-IR/submm wavelengths, by producing model HERUS-like catalogues for the various possibilities and then fitting a single temperature (T, β) model to them using the same MCMC code described above. The simulated HERUS fluxes have Gaussian noise added to them matching the average signal-to-noise ratio of the appropriate HERUS band before the fitting process.

The possibility of hot dust contamination at short wavelengths is modelled by adding a 100K $\beta = 1.7$ dust component to an underlying (T, $\beta = 1.7$) SED with temperatures ranging from 30 to 60K. $\beta = 1.7$ is chosen since this is the average β value for the HERUS sample. The strength of this hot dust contribution was varied up to a maximum of 50 per cent of the flux in the 60 μm band. Cold dust contamination is modelled in a similar way, by adding a 20K $\beta = 1.7$ component to a similar range of underlying templates, but with the contribution normalized to some fraction of the 250 μm flux, rising once again to a maximum of 50 per cent of the 250 μm flux. The possibility of optically thick dust was modelled with a thermal dust SED with temperature ranging from 30 to 60K and a β of 1.7 but which has an optical depth of 1 at 200 μm. This is similar to the dust SED found for Arp220 by Rangwala et al. (2011).

None of these simple, uniform, models for the underlying SED reproduces what is seen in the data. Neither of the hot or cold additional dust component models can reproduce fractional residuals as large as those seen, even when the additional component makes up 50 per cent of the flux of the appropriate normalization band (60 μm for hot dust and 250 μm for cold). The optically thick model also fails to reproduce the size of the residuals. Furthermore, none of the models could reproduce the pattern of residuals, where we see similar, negative, residuals in the three SPIRE bands that are all uncorrelated with fitted temperature, and positive residuals correlated with temperature in the *IRAS* bands. Better sampling of the far-IR SEDs of ULIRGs so that we can determine the properties of each individual object will be necessary to make progress on this problem.

6.2 Far-IR colours

Although fitting models to the SEDs of *Herschel* sources is one way to compare different populations, another is simply to compare their far-IR colours. In Fig. 9, we show the 100-to-250 μm and 350-to-500 μm colours of the HERUS sources, HRS sources, and those Magdis et al. (2014) sources where 100 μm fluxes are available. The H-ATLAS sources lie in the same region as the bulk of the HRS spiral-type galaxies. However, the HERUS ULIRGs lie in an almost completely separate part of the colour–colour diagram to the HRS sources or the Magdis et al. ULIRGs. Only one HRS source lies in the HERUS ULIRG region – NGC4697 – classified as a post-merger remnant elliptical (e.g. Arnold et al. 2014) hosting a low luminosity AGN (Yuan, Yu & Ho 2009). Similarly, only one Magdis ULIRG for which 100 μm fluxes are available, CDFS2, lies

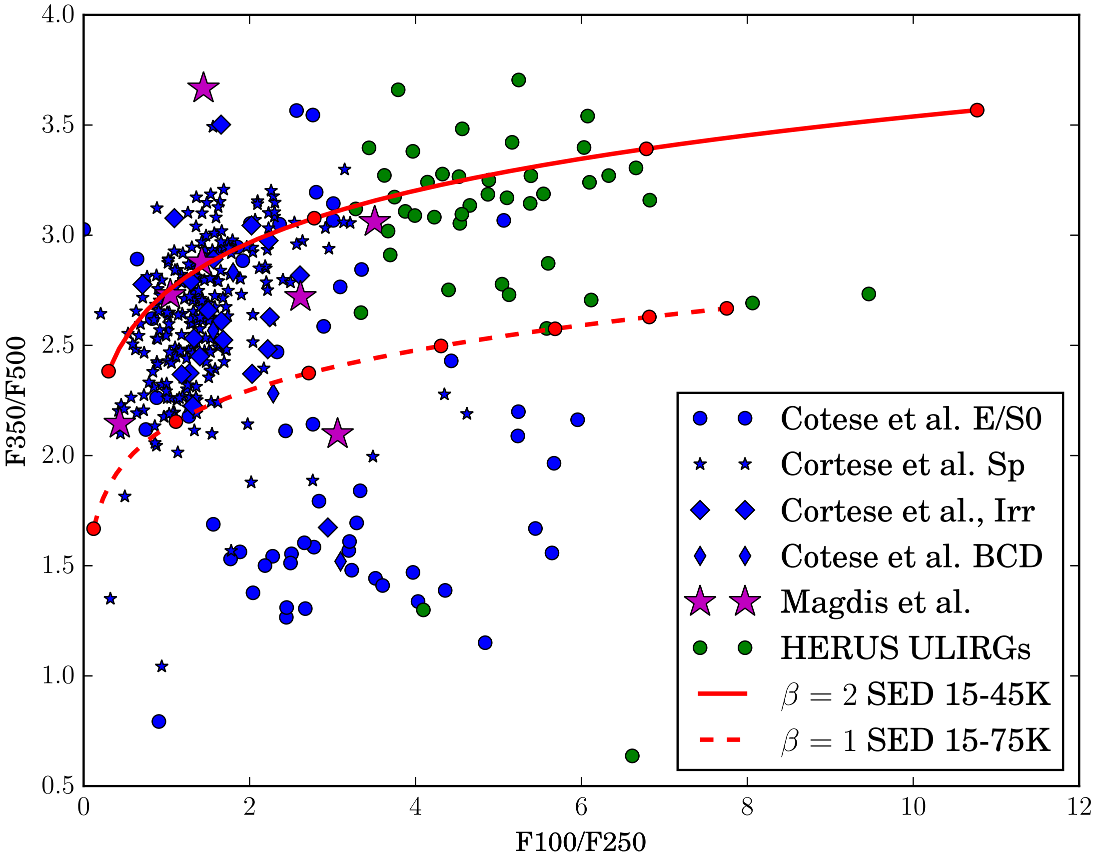

Figure 9. The colours of HERUS ULIRGs compared to other samples. *F100/F250* versus *F350/F500* shown for HERUS ULIRGs (green dots), HRS galaxies (blue symbols) of different morphological types (E and S0 dots, Spiral stars, Irr and Pec broad diamonds, blue compact dwarfs narrow diamonds), and Magdis ULRGs where data is available (magenta stars). Also plotted are lines showing the colours of modified blackbody spectra with $\beta = 2$ (solid) from 15 to 45K and $\beta = 1$ (dashed) going from 15K to 75K. Solid dots along these lines indicate temperatures in increments of 10K starting at 15K at the left-hand side of the plot. The H-ATLAS 250 µm sources occupy the same region of the diagram as the bulk of the Cortese et al. (2014) HRS sources. Note that the IRAS-selected ULIRGs and the Magdis 250 µm selected sources have an almost disjoint range of colours, and that the Magdis sources have colours much more typical of local star forming galaxies from HRS.

close to the HERUS ULIRG region. The Magdis et al. ULIRGs with measured 100 µm fluxes plotted here lie at redshifts from 0.21 to 0.35, whereas the highest redshift HERUS ULIRG is at $z = 0.26$. The two samples thus overlap in redshifts, so K-corrections and evolution will not be responsible for the differences we are seeing. The HERUS ULIRGs were selected at 60 µm, whereas the Magdis ULIRGs were selected at 250 µm. We also note that the HRS spirals have comparable colours to the overall population of 250-µm selected galaxies in H-ATLAS.

We also plot colour tracks for two simple (T, β) models, one with $\beta = 2$ and the other with $\beta = 1$, and temperature ranging from 15 to 45K for the former and 15 to 75K for the latter. Most galaxies in this plot appear to be scattered between these two lines with the HRS and Magdis sources having lower temperatures than the HERUS ULIRGs. A small fraction of HRS sources, largely E and S0 types, lie below the $\beta = 1$ line, as does one of the Magdis ULIRGs and two of the HERUS sources. These latter are 3c273 and IRAS 13451+1232, whose far-IR SEDs are dominated by non-thermal emission. This may well be the case for the other sources in this part of the diagram. The most extreme HERUS sources on the right-hand side of this diagram are IRAS 08572+3915 and IRAS 01003−2238, which both lie on a rightwards extension of the $\beta = 1$ track to higher temperatures (though their best SED fits have β values closer to 2). Both of these sources are known to contain dust obscured AGNs (Imanishi et al. 2007; Efstathiou et al. 2014). The other HERUS source lying on the $\beta = 1$ line at somewhat lower temperature is Mrk463, which also hosts an AGN.

It is tempting to envisage a potential evolutionary track in this diagram whereby two cooler dust galaxies close to the locus of HRS spiral-type galaxies merge, triggering a starburst that warms their dust and moves the merging system towards the HERUS ULIRG region along the $\beta = 2$ line. The merger also funnels gas into the nuclear regions of the merging galaxy, fuelling an AGN. As the starburst ages and the AGNs become more significant, the merger moves away from the $\beta = 2$ line towards the $\beta = 1$ line. In this context, it is interesting to note that the Magdis et al. ULIRGs have a similar $L_{[\mathrm{C\,II}]}/L_{\mathrm{FIR}}$ ratio to normal star-forming galaxies, which they are closer to in this colour–colour diagram, than do local *IRAS* selected ULIRGs, which appear to be [C II] deficient (Farrah et al. 2013).

6.3 ULIRG selection functions

Although evolutionary state and/or AGN content is a possible explanation for the difference between the HERUS and Magdis ULIRGs, another plausible explanation is the possibility that the different wavelengths at which these sources are selected – 60 µm in the case of the HERUS ULIRGs and 250 µm in the case of the Magdis

ULIRGs, and the H-ATLAS galaxies that have similar colours – might lead to systematic biases in the types of sources found by these different surveys. To examine this, we select two of the panchromatic SEDs for *Herschel* sources provided by Berta et al. (2013), one matching the average colour of the HERUS ULIRGs and the other matching that of the HRS sources and Magdis ULIRGs. We then look at how the observed flux of such a template source with a luminosity of $10^{12}\,\mathrm{L}_{\odot}$ varies with redshift and compare this to the selection criteria used for HERUS at 60 µm and in Magdis et al. (2014) at 250 µm.

The Berta templates selected were the cold galaxy (template 2 in the Berta template library) for 250 µm selected sources, matching average colours of *F100/F250* ∼ 1.5 and *F350/F500* ∼ 2.7, and the obscured star-forming galaxy (template 8 in the template library) for *IRAS* selected ULIRGs, matching their average colour of *F100/F250* ∼ 5 and *F350/F500* ∼ 3. There is a substantial scatter in the colours of these different samples so these specific templates will not give a perfect match to the data. Nevertheless, they can provide insights into any major differences resulting from the selection of sources with such different colours at different wavelengths (see also fig. 5 of Magdis et al. 2014).

The flux versus redshift for these templates for a $10^{12}\,\mathrm{L}_{\odot}$ source, together with the selection functions for the HERUS ($S_{60} > 1.8$ Jy and $z < 0.3$) and Magdis samples ($S_{250} > 0.15$Jy and $0.9 > z > 0.21$), as well as the fluxes and redshifts for the sources in these samples are shown in Fig. 10. As can be seen, for selection at 60 µm, the warmer SED sources are marginally favoured since, at any given redshift, they are somewhat brighter than the cold SED sources, by a factor of about 1.5. However, for selection at 250 µm, the situation is very different. A cold SED source will be substantially brighter at 250 µm than a hot SED source, by a factor of up to an order of magnitude, out to redshifts of 1–2. A hot SED source would have to be much more luminous to be selected at a given 250 µm flux than a cold SED source.

Fig. 10 also shows how selection at 250 µm would affect the HERUS sample if it were shifted to higher redshifts. To do this, we use the fitted HERUS SEDs to predict the 250 µm flux of each of our sources if it were shifted to a redshift of 0.56, at the centre of the redshift range of the main Magdis et al. selection. These sources are shown in red. Not one of them would have been bright enough for inclusion in the Magdis sample. Significantly more-luminous IRAS-type, 60 µm selected ULIRGs could still be selected at 250 µm, but since the luminosity function at 250 µm declines steeply at these luminosities (e.g. Marchetti et al. 2016), the number density of such sources is very low. We also perform a similar analysis on the Magdis ULIRGs to see how many would be selected by *IRAS* at 60µm if they were at the mean redshift of the HERUS sample, $z = 0.1$. Here, we find that roughly half of the Magdis sources would be detected by *IRAS* at this redshift.

The comoving volume of the *IRAS* survey is much larger than that of the Magdis et al. survey. The parent catalogue on which HERUS is based covers an area of 16 300 deg^2 and our selection reaches out to $z = 0.3$, yielding a total comoving volume of $3\,\mathrm{Gpc}^3$. The Magdis survey covers 100 deg^2 and a redshift range of 0.21–0.9, for a comoving volume of $0.3\,\mathrm{Gpc}^3$. If we ignore evolution, and assume that 250 µm selected ULIRGs have the same comoving density in the local Universe as they are observed to have in the Magdis survey, there should be 70 such objects seen by *IRAS* that would have been included in the HERUS survey, when there are in fact none.

However, it has long been known that the ULIRG population strongly evolves with redshift. If we assume that the Magdis ULIRGs evolve at the same rate as the general ULIRG population, whose number density n has been found to evolve as $n \propto (1 + z)^n$ with $n = 7.05^{+0.25}_{-0.18}$ (Patel 2012, which presents an improved determination of this parameter from Patel et al. 2013; see also Kim & Sanders 1998), then their number density is reduced by a factor of 11.75 from $z = 0.56$, the mean redshift of the Magdis survey, to 0.1, the mean redshift of the HERUS sample. The expected number of Magdis ULIRGs in the HERUS sample would then be 6. If the two classes were entirely distinct, this would represent a $\sim 2.4\sigma$ discrepancy, which, while intriguing, is not a formally significant result. However, since there is not a solid boundary between the two classes, with some cross-over at *F100/F250* ∼ 4 (see Fig. 9) then the significance of this difference falls still further, and we conclude that the Magdis-type ULIRGs are too rare in the local Universe for the existing 60 µm selected *IRAS* surveys to pick them up in significant numbers.

We thus conclude, it is possible that the apparent dichotomy drawn between low z *IRAS* selected ULIRGs and the higher z, 250-µm selected ULIRGs in Magdis et al. (2014), with the lower redshift objects showing [C II] deficiency, more intense excitation (Rigopoulou et al. 2014) and smaller star-forming regions (Díaz-Santos et al. 2013), might be a result of selection at different wavelengths and not indicate very rapid evolution in the properties of the ULIRG population. Searches for ULIRG-luminosity objects with cool dust SEDs in the local Universe, possibly using the *IRAS* 100-µm catalogue or the AKARI 140-µm catalogue as a starting point, and for warm dust ULIRGs at higher redshifts, possibly using PACS data, may be able to test this idea. Further study of intermediate redshift ULIRG samples (e.g. Combes et al. 2011) may also be very useful.

7 CONCLUSIONS

We present a far-IR photometric atlas of local *IRAS* selected ULIRGs from the HERUS survey, including fluxes and images at 250, 350, and 500 µm, derived from observations with the SPIRE instrument on the *Herschel Space Observatory* together with images of these sources in the three respective wavebands. We fit the SEDs of these sources using a simple optically thin dust SED and derive temperatures and emissivity parameter β. We find that the dust temperatures in our sources are significantly higher than the dust temperatures of lower luminosity sources, but that the distribution of emissivity parameters is similar. We compare the temperature and luminosity of our sources to those of far-IR emitting galaxies at a wide range of luminosities and redshifts, finding that while high redshift SMGs still appear colder than local ULIRGs of a similar luminosity, the distinction between these samples is becoming less distinct as more sources are observed. A comparison of the far-IR colours of our sources and lower luminosity objects from the literature uncovers an unexpected dichotomy between our ULIRGs, lower luminosity systems, and ULIRGs selected at longer wavelengths using the SPIRE 250-µm band. This difference may result from selection at different wavelengths, with 250-µm selection biased in favour of selecting sources with a cooler SED over a wide range of redshifts.

The next steps for SED studies of local ULIRGs are to use a wider range of existing photometric data to study the far-IR SEDs in more detail through fitting more complex models. Extant other far-IR to submm data, however, unlike that presented in this paper, is inhomogeneous, with some famous sources, such as Arp220 or Mrk231, observed in many more bands than some of the less well-studied objects.

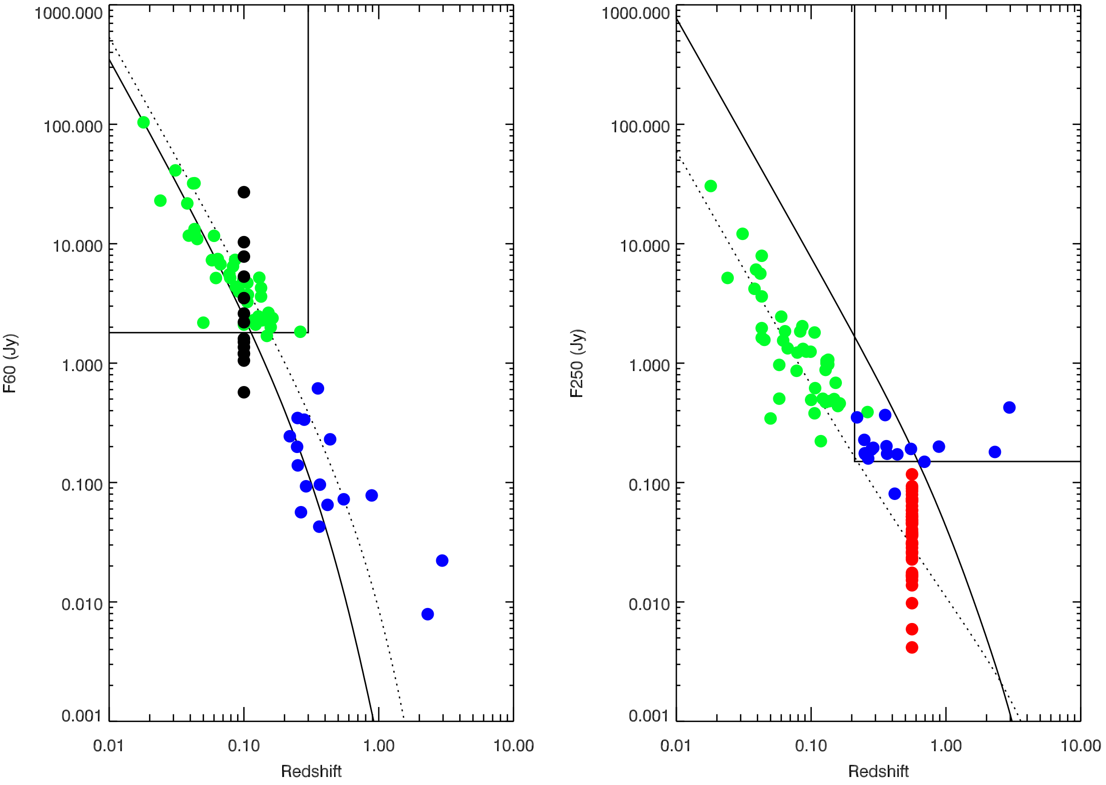

Figure 10. Flux of a 10^{12} $L_\odot$ galaxy as a function of redshift at 60 μm (left-hand panel) and 250 μm (right-hand panel) as derived from the Berta et al. (2013) templates. Solid line is for a cold galaxy, appropriate for the 250 μm selected Magdis et al. objects, dotted line is for an obscured star forming galaxy, appropriate for an *IRAS* selected ULIRG. Dots show the fluxes and redshifts for the HERUS ULIRGs (green) and the Magdis et al. ULIRGs (blue – we use the 70 μm fluxes for these sources since 60 μm fluxes are not available). Solid lines indicate the selection functions of this work on the 60 μm plot and of Magdis et al. on the 250 μm plot. Note that the cold galaxy template is about an order of magnitude brighter at 250 μm than the obscured star-forming galaxy at any given redshift for the same luminosity, whereas at 60 μm, the fluxes are about the same. This will lead to the selection of significantly different objects at 250 μm at any given flux limit. The red points in the right-hand hand plot indicate the 250 μm fluxes that the HERUS sources would have if they were redshifted to $z = 0.56$. None would be bright enough at 250μm to be selected by Magdis et al. The black points in the left-hand hand plot indicate the 60 μm fluxes of Magdis et al. sources if they were at a redshift of 0.1. Half of the sample, seven galaxies, would be selected by the HERUS criteria.

ACKNOWLEDGEMENTS

SPIRE has been developed by a consortium of institutes led by Cardiff University (UK) and including: University of Lethbridge (Canada); NAOC (China); CEA, LAM (France); IFSI, University of Padua (Italy); IAC (Spain); Stockholm Observatory (Sweden); Imperial College London, RAL, UCL-MSSL, UKATC, University of Sussex (UK); and Caltech, JPL, NHSC, University of Colorado (USA). This development has been supported by national funding agencies: CSA (Canada), NAOC (China), CEA, CNES, and CNRS (France), ASI (Italy), MCINN (Spain), SNSB (Sweden), STFC, UKSA (UK), and NASA (USA). HIPE is a joint development by the *Herschel* Science Ground Segment Consortium, consisting of ESA, the NASA *Herschel* Science Centre, and the HIFI, PACS and SPIRE consortia. This research has made use of the NASA/IPAC Extragalactic Database (NED), which is operated by the Jet Propulsion Laboratory, California Institute of Technology, under contract with the National Aeronautics and Space Administration. EG-A is a Research Associate at the Harvard–Smithsonian Center for Astrophysics, and thanks the Spanish Ministerio de Economía y Competitividad for support under projects FIS2012-39162-C06-01 and ESP2015-65597-C4-1-R, and NASA grant ADAP NNX15AE56G. JB-S wishes to acknowledge the support of a Career Integration Grant within the 7th European Community Framework Program, FP7-PEOPLE-2013-CIG-630861-FEASTFUL. JA acknowledges financial support from the Science and Technology Foundation (FCT, Portugal) through research grants PTDC/FIS-AST/2194/2012 and UID/FIS/04434/2013. DLC and JG acknowledge support from STFC, in part through grant numbers ST/N000838/1 and ST/K001051/1. The authors wish to thank A. Jaffe and D. Smith for useful conversations, and the anonymous referee for their comments. This paper is based in part on observations with *Herschel*, an ESA space observatory with science instruments provided by European-led Principal Investigator consortia and with important participation from NASA.

REFERENCES

Abazajian K. N. et al., 2009, ApJS, 182, 543
Arnold J. A. et al., 2014, ApJ, 791, 80
Bendo G. J. et al., 2003, AJ, 125, 2361
Bendo G. J. et al., 2013, MNRAS, 433, 3062
Berta S. et al., 2013, A&A, 551, A100
Chapman S. C., Blain A. W., Smail I., Ivison R. J., 2005, ApJ, 622, 772
Ciesla L. et al., 2014, A&A, 565, A128
Clements D. L., Andreani P., Chase S. T., 1993, MNRAS, 261, 299
Clements D. L., Sutherland W. J., McMahon R. G., Saunders W., 1996, MNRAS, 279, 477
Clements D. L., Dunne L., Eales S., 2010, MNRAS, 403, 274

Combes F., García-Burillo S., Braine J., Schinnerer E., Walter F., Colina L., 2011, A&A, 528, A124
Cortese L. et al., 2014, MNRAS, 440, 942
Díaz-Santos T. et al., 2013, ApJ, 774, 68
Dole H. et al., 2001, A&A, 372, 364
Dole H. et al., 2006, A&A, 451, 417
Dowell C. D. et al., 2010, in Oschmann J. M., Jr, Clampin M. C., MacEwen H. A. >Proc. SPIE Conf. Ser. Vol. 7731, Space Telescopes and Instrumentation 2010: Optical, Infrared, and Millimeter Wave. SPIE, Bellingham, p. 773136
Draine B. T., 2003, ARA&A, 41, 241
Driver S. P. et al., 2011, MNRAS, 413, 971
Duc P.-A., Mirabel I. F., Maza J., 1997, A&AS, 124, 533
Dunne L., Eales S. A., 2001, MNRAS, 327, 697
Dunne L., Eales S., Edmunds M., Ivison R., Alexander P., Clements D. L., 2000, MNRAS, 315, 115
Eales S. et al., 2010, PASP, 122, 499
Efstathiou A., Siebenmorgen R., 2009, A&A, 502, 541
Efstathiou A. et al., 2014, MNRAS, 437, L16
Farrah D. et al., 2001, MNRAS, 326, 1333
Farrah D., Afonso J., Efstathiou A., Rowan-Robinson M., Fox M., Clements D., 2003, MNRAS, 343, 585
Farrah D. et al., 2006, ApJ, 641, L17
Farrah D. et al., 2013, ApJ, 776, 38
Fischer J. et al., 2010, A&A, 518, L41
Fischer J., Abel N. P., González-Alfonso E., Dudley C. C., Satyapal S., van Hoof P. A. M., 2014, ApJ, 795, 117
Foreman-Mackey D., Hogg D. W., Lang D., Goodman J., 2013, PASP, 125, 306
González-Alfonso E. et al., 2015, ApJ, 800, 69
González-Alfonso E. et al., 2017, ApJ, 836, 11
Griffin M. J. et al., 2010, A&A, 518, L3
Gruppioni C. et al., 2013, MNRAS, 432, 23
Hopkins P. F., 2012, MNRAS, 420, L8
Hou L. G., Han J. L., Kong M. Z., Wu X.-B., 2011, ApJ, 732, 72
Huang J.-S. et al., 2014, ApJ, 784, 52
Hughes D. H. et al., 1998, Nature, 394, 241
Imanishi M., Dudley C. C., Maiolino R., Maloney P. R., Nakagawa T., Risaliti G., 2007, ApJS, 171, 72
Janssen A. W. et al., 2016, ApJ, 822, 43
Jaynes E. T., 2003, Probability Theory - The Logic of Science. Cambridge Univ. Press, Cambridge
Kim D. C., Sanders D. B., 1998, ApJS, 119, 41
Klaas U., Haas M., Müller S. A. H. et al., 2001, A&A, 379, 823
Köhler M., Ysard N., Jones A. P., 2015, A&A, 579, 15
Lewis A., Bridle S., 2002, Phys. Rev. D, 66, 103511
Magdis G. E. et al., 2014, ApJ, 796, 63
Marchetti L. et al., 2016, MNRAS, 456, 1999
Oliver S. J. et al., 2012, MNRAS, 424, 1614
Patel H., 2012, PhD thesis, Imperial College London
Patel H., Clements D. L., Vaccari M., Mortlock D. J., Rowan-Robinson M., Pérez-Fournon I., Afonso-Luis A., 2013, MNRAS, 428, 291
Pearson C., Lim T., North C. et al., 2014, Exp. Astron., 37, 175
Pearson C. et al., 2016, ApJS, 227, 9
Pereira-Santaella M., Rigopoulou D., Farrah D., Lebouteiller V., Li J., 2017, MNRAS, 470, 1218
Pilbratt G. et al., 2010, A&A, 518, L1
Planck Collaboration XVI, 2011, A&A, 536, A16
Poglitsch A. et al., 2010, A&A, 518, L2
Rangwala N. et al., 2011, ApJ, 743, 94
Rigopoulou D., Spoon H. W. W., Genzel R., Lutz D., Moorwood A. F. M., Tran Q. D., 1999, AJ, 118, 2625
Rigopoulou D., Hopwood R., Magdis G. E. et al., 2014, ApJ, 781, L15
Sanders D. B., Mirabel I. F., 1996, ARA&A, 34, 725
Sanders D. B., Soifer B. T., Elias J. H., Madore B. F., Matthews K., Neugebauer G., Scoville N. Z., 1988a, ApJ, 325, 74
Sanders D. B., Soifer B. T., Elias J. H., Neugebauer G., Matthews K., 1988b, ApJ, 328, L35
Saunders W. et al., 2000, MNRAS, 317, 55
Savage R., Oliver S., 2007, ApJ, 661, 1339
Smail I., Ivison R. J., Blain A. W., 1997, ApJ, 490, L5
Smith D. J. B. et al., 2013, MNRAS, 436, 2435
Soifer B. T., Neugebauer G., Helou G. et al., 1984, ApJ, 283, L1
Spoon H. W. W. et al., 2013, ApJ, 775, 127
Sturm E. et al., 2011, ApJ, 733, L16
Veilleux S. et al., 2013, ApJ, 776, 27
Vlahakis C., Dunne L., Eales S., 2005, MNRAS, 364, 1253
Wright G. S., Joseph R. D., Meikle W. P. S., 1984, Nature, 309, 430
Yang M., Greve T. R., Dowell C. D., Borys C., 2007, ApJ, 660, 1198
Ysard N., Köhler M., Jones A., Miville-Deschênes M.-A., Abergel A., Fanciullo L., 2015, A&A, 577, A110
Yuan F., Yu Z., Ho L. C., 2009, ApJ, 703, 1034

APPENDIX A: SPIRE IMAGES OF HERUS SOURCES

This appendix presents the SPIRE images of the HERUS ULIRGs at 500, 350, and 250 μm.

Notes on specific images:

IRAS03521+0028: There is a significant extended structure in the far-IR sky near this source, which can be seen in the background of the SPIRE maps of this object. This is visible in the wider field *IRAS* 60 and 100 μm maps. Nevertheless, the source is compact and well localized so this structure, likely a result of galactic foregrounds, has no impact on the photometric accuracy for this source.

IRAS06035−7102: This image is based on a cut-out of the larger SPIRE survey of the LMC. It thus has a somewhat different format to the other images, which show the full SPIRE small scan map around the target ULIRG.

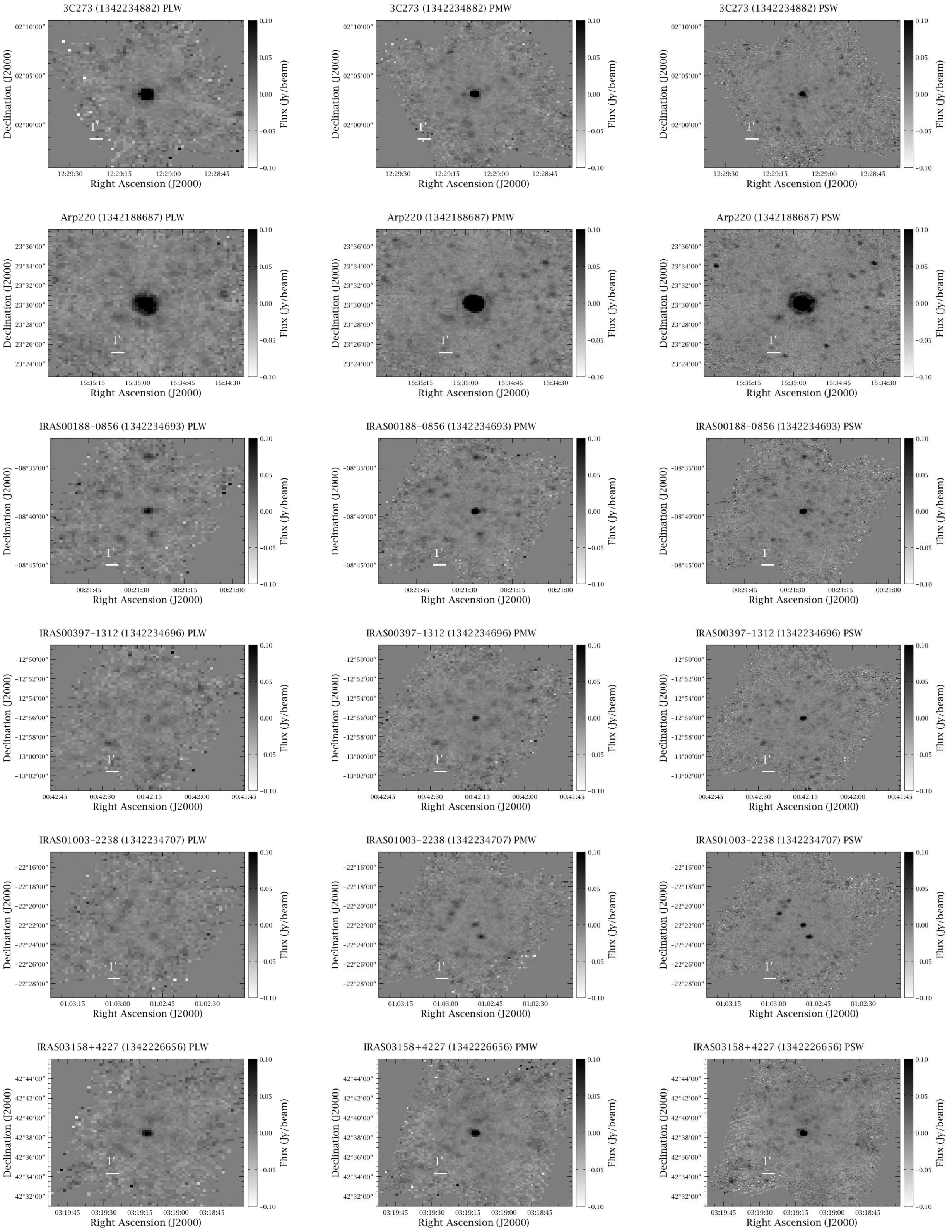

Figure A1. SPIRE images of the HERUS ULIRGs at 500, 350, and 250 μm going from left- to right-hand side.

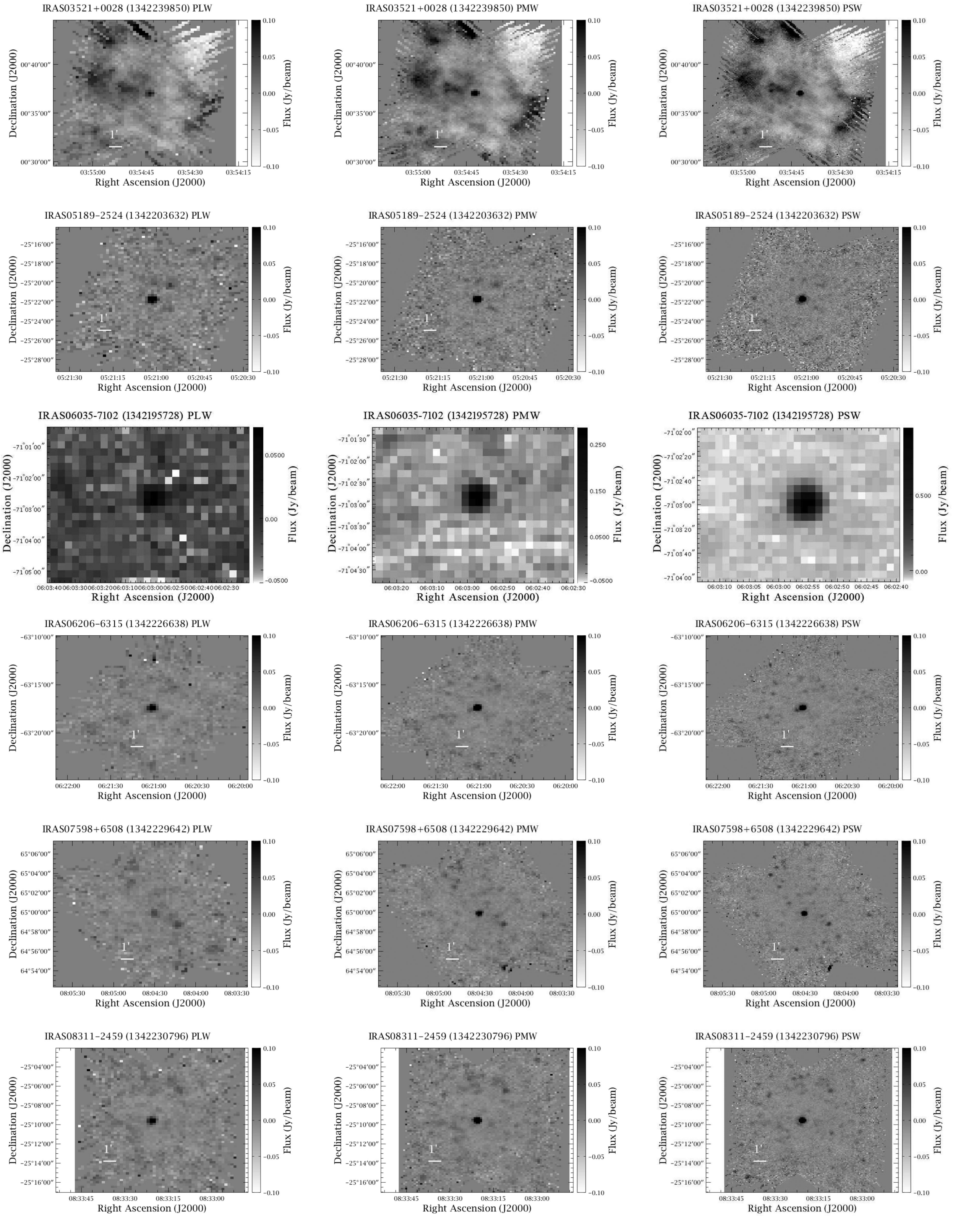

Figure A1 – *continued*

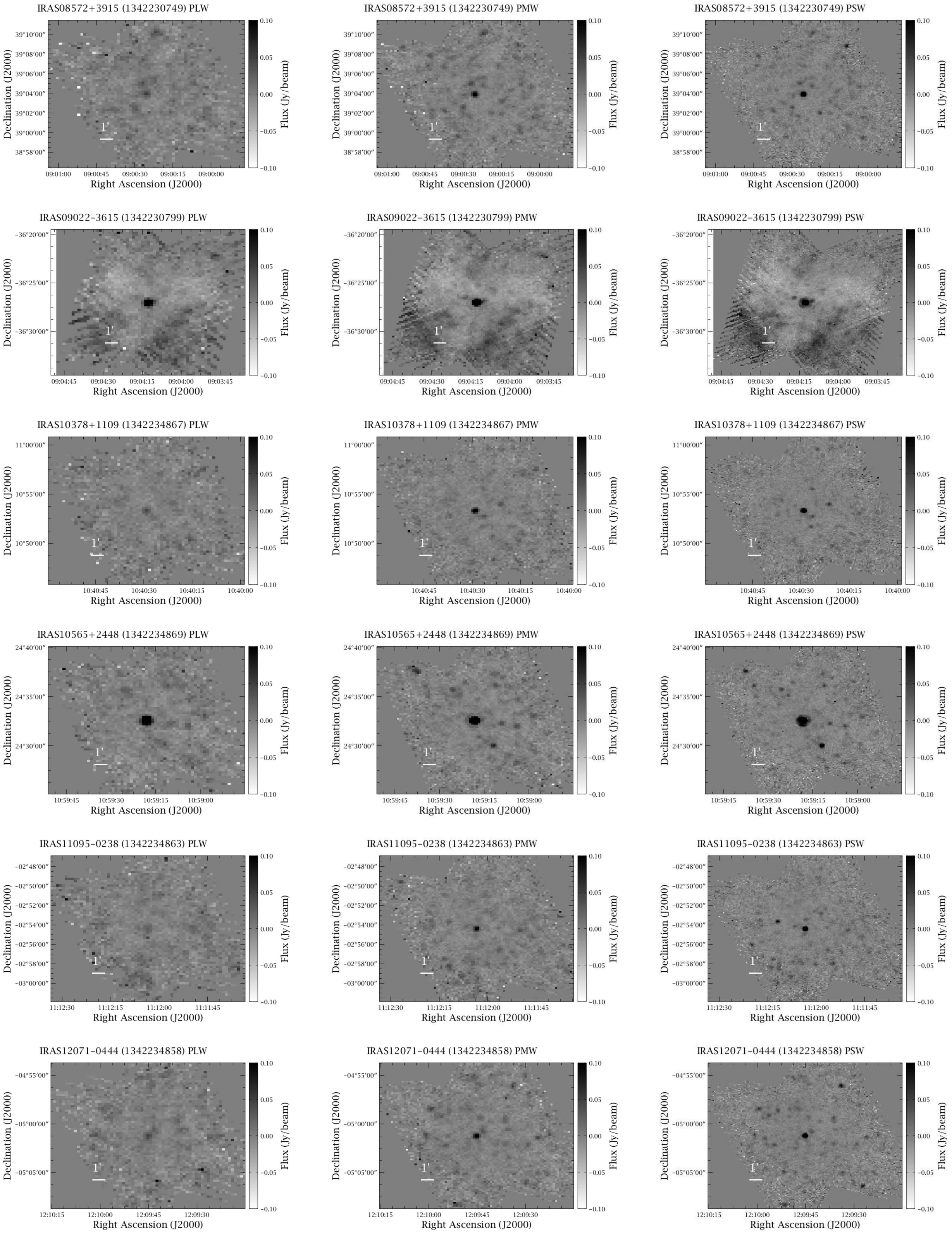

Figure A1 – *continued*

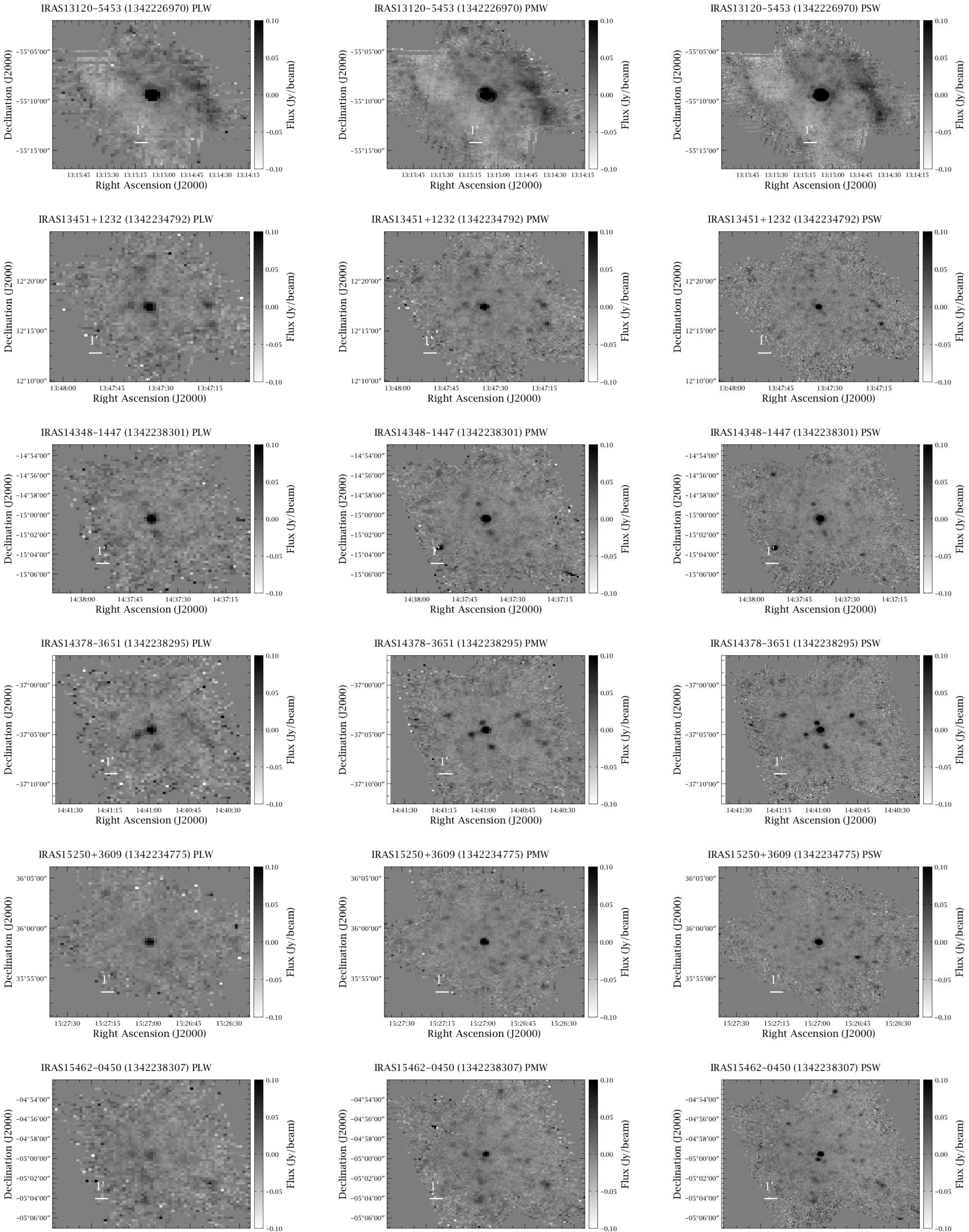
IRAS13120−5453 (1342226970) PLW
IRAS13120−5453 (1342226970) PMW
IRAS13120−5453 (1342226970) PSW
IRAS13451+1232 (1342234792) PLW
IRAS13451+1232 (1342234792) PMW
IRAS13451+1232 (1342234792) PSW
IRAS14348−1447 (1342238301) PLW
IRAS14348−1447 (1342238301) PMW
IRAS14348−1447 (1342238301) PSW
IRAS14378−3651 (1342238295) PLW
IRAS14378−3651 (1342238295) PMW
IRAS14378−3651 (1342238295) PSW
IRAS15250+3609 (1342234775) PLW
IRAS15250+3609 (1342234775) PMW
IRAS15250+3609 (1342234775) PSW
IRAS15462−0450 (1342238307) PLW
IRAS15462−0450 (1342238307) PMW
IRAS15462−0450 (1342238307) PSW

Figure A1 – *continued*

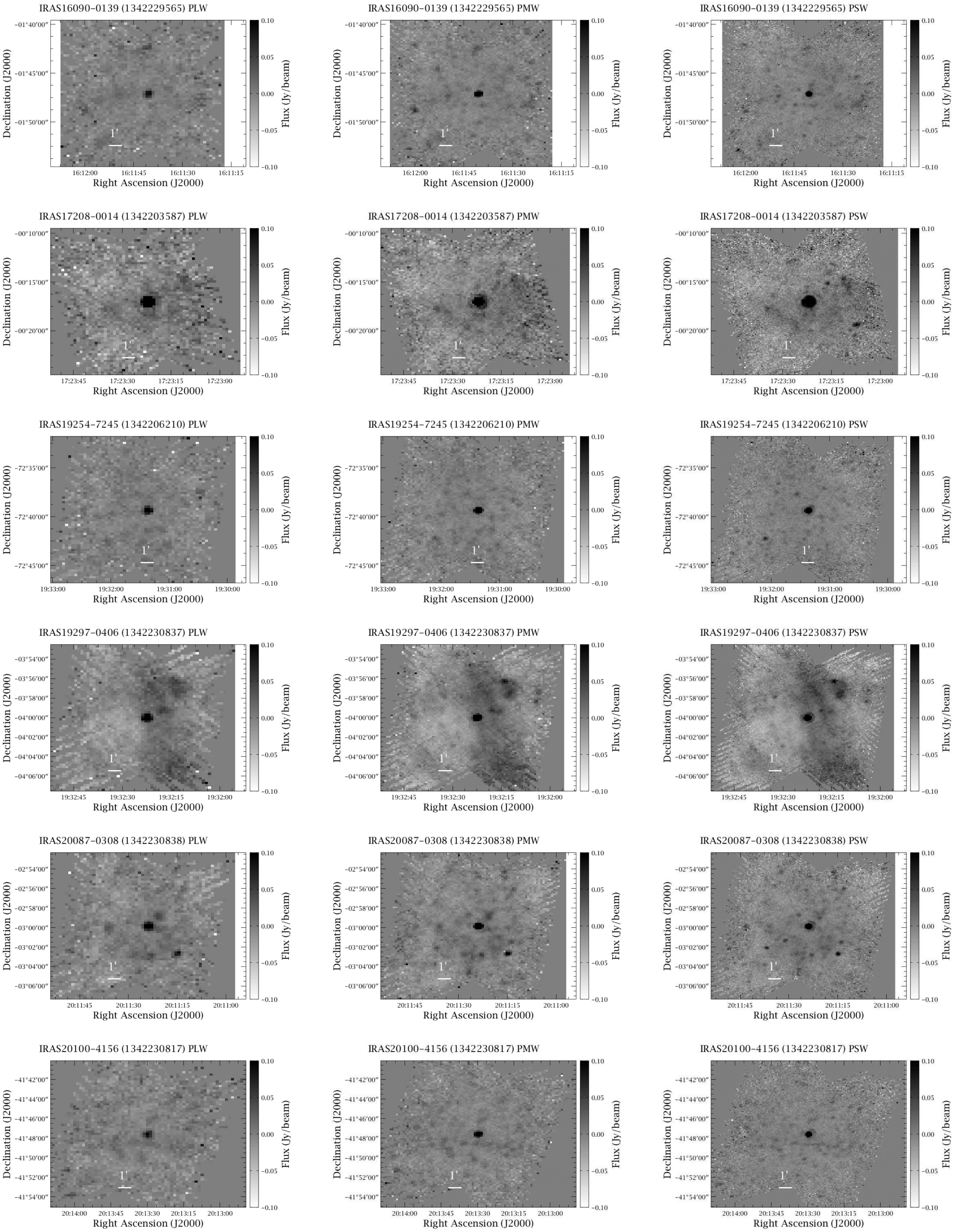

Figure A1 – *continued*

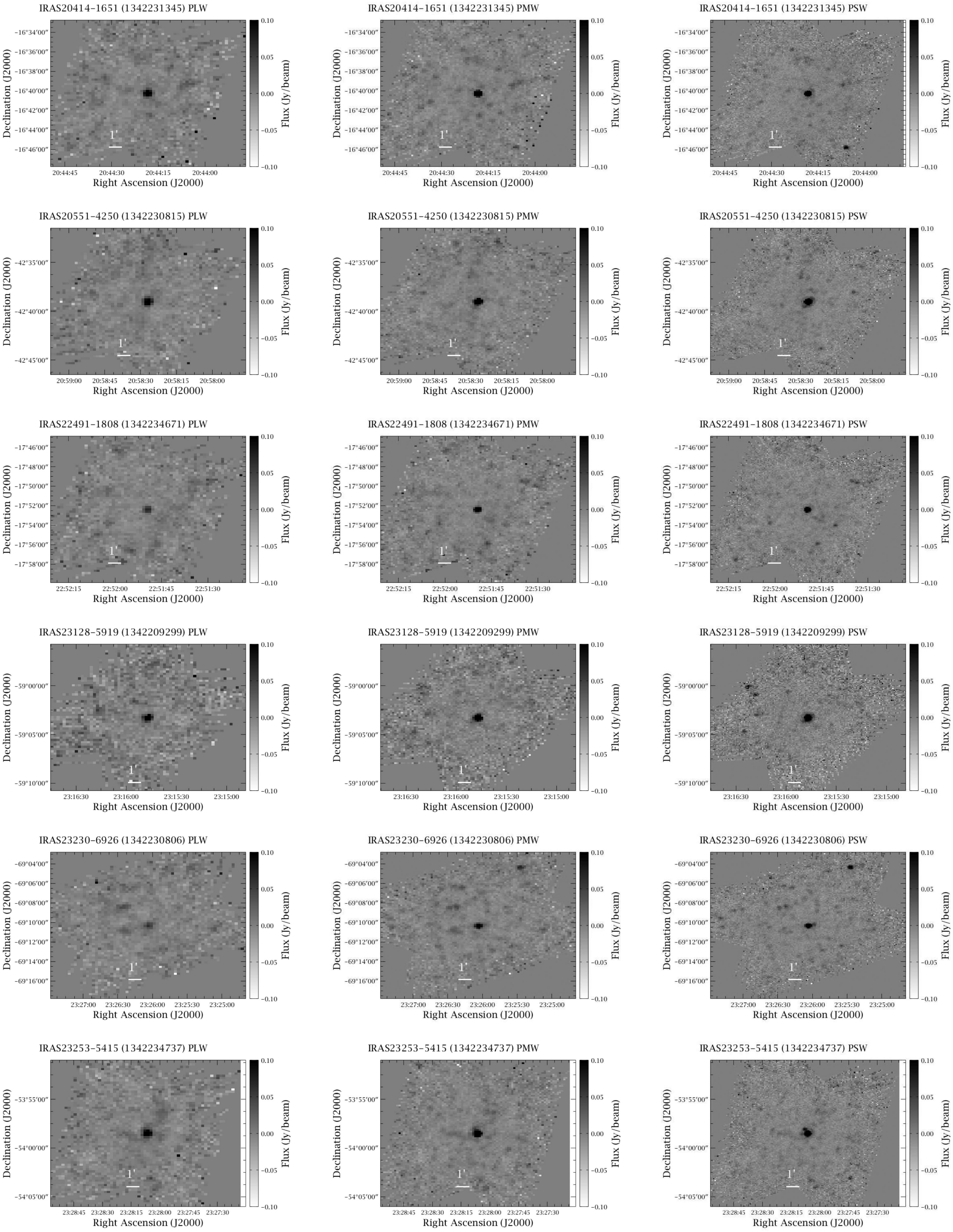

Figure A1 – *continued*

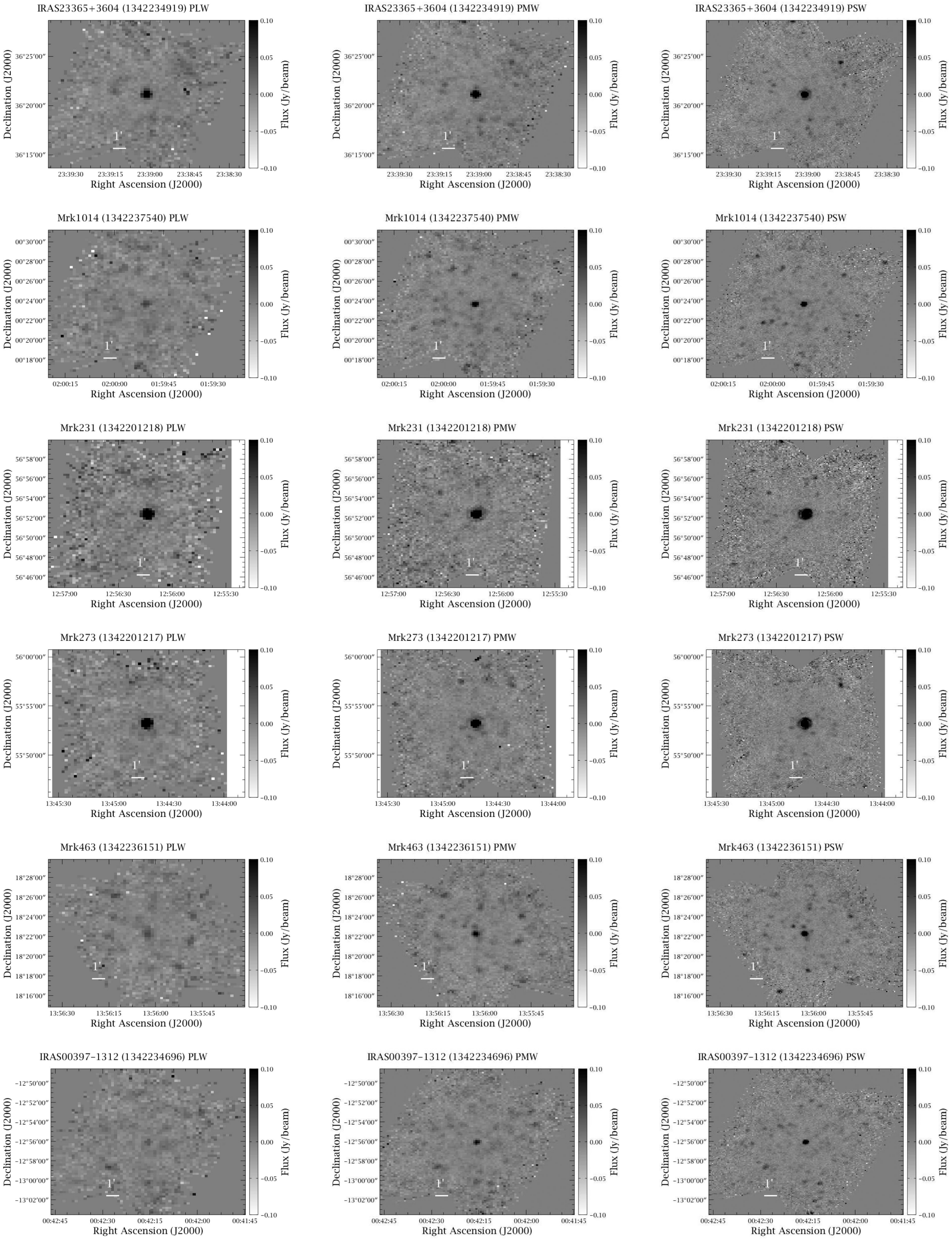

Figure A1 – *continued*

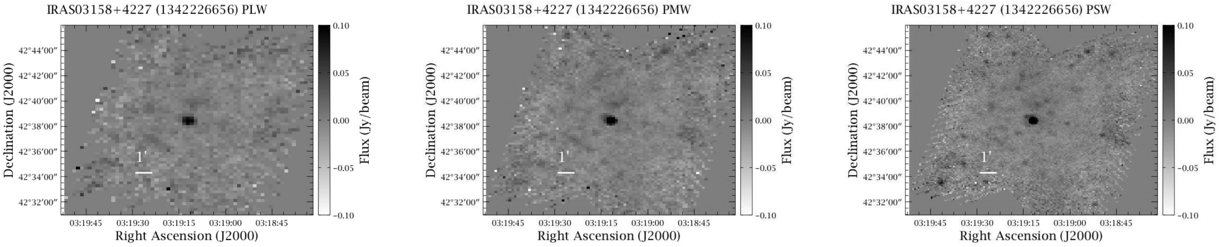

Figure A1 – *continued*

APPENDIX B: SED FITS COMPARED TO THE OBSERVATIONAL DATA.

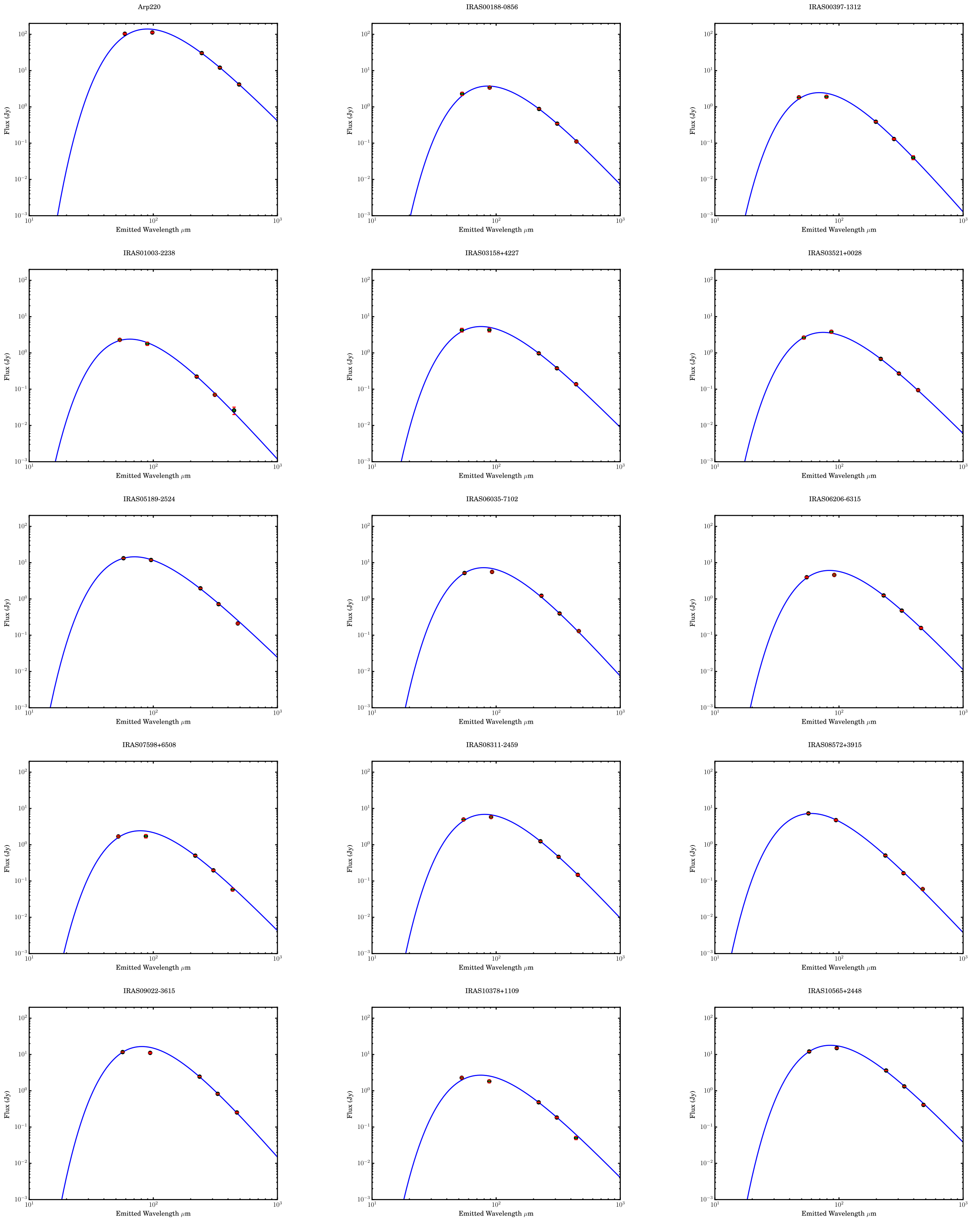

Figure B1. Fitted SEDs compared to the observational data from IRAS and SPIRE. Fit is shown as the blue line, data points as green dots. Error bars on the fluxes are also shown (in red) but are generally smaller than the green dots of the data points.

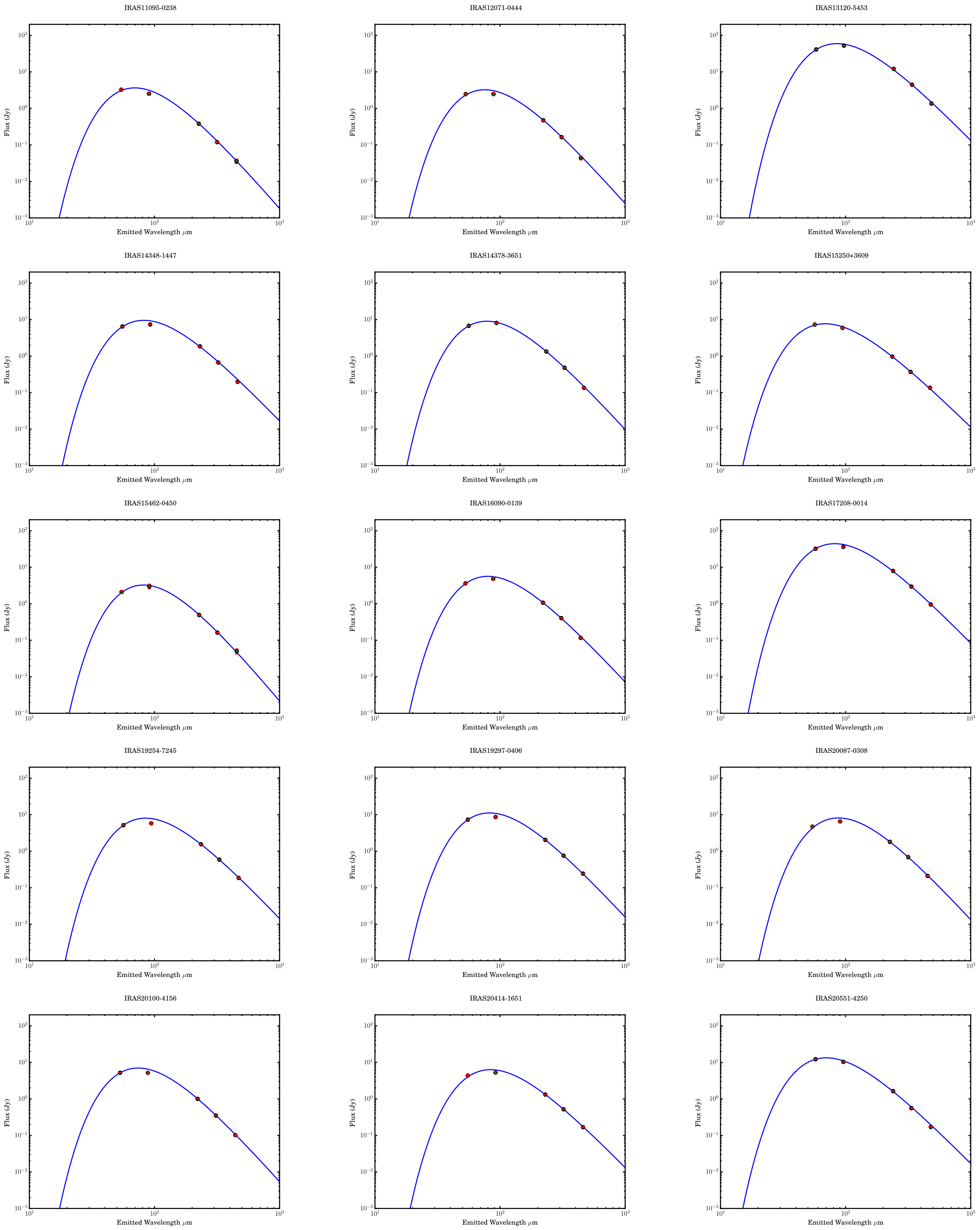

IRAS11095-0238 IRAS12071-0444 IRAS13120-5453

IRAS14348-1447 IRAS14378-3651 IRAS15250+3609

IRAS15462-0450 IRAS16090-0139 IRAS17208-0014

IRAS19254-7245 IRAS19297-0406 IRAS20087-0308

IRAS20100-4156 IRAS20414-1651 IRAS20551-4250

Figure B1 – *continued*

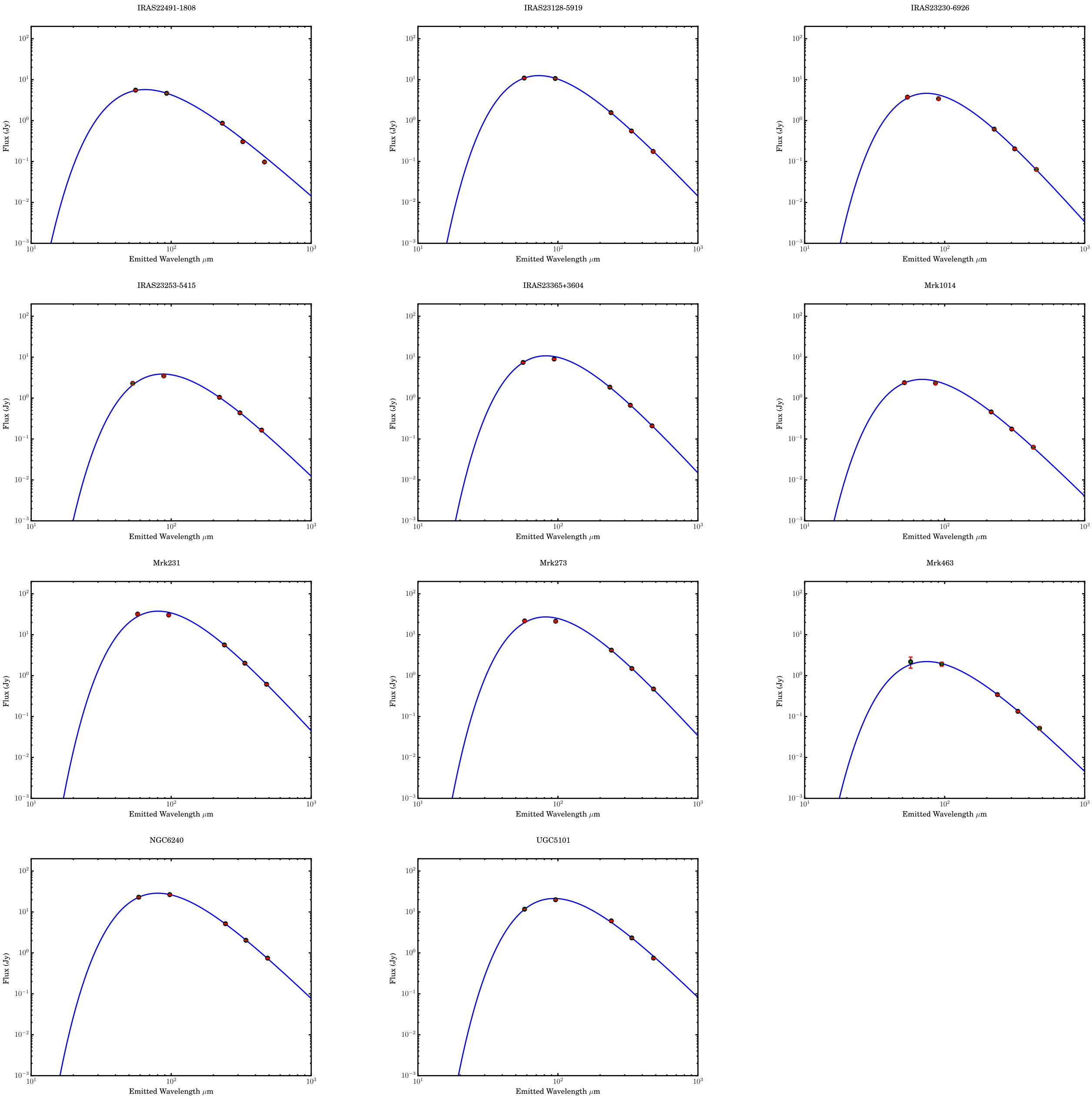

Figure B1 – *continued*

This paper has been typeset from a TEX/LATEX file prepared by the author.